Key Engineering Materials Vols. 153-154 (1998) pp. 143-182

Plastic Deformation of Cubic Zirconia Single Crystals

U. Messerschmidt, B. Baufeld and D. Baither

Max Planck Institute of Microstructure Physics, Weinberg 2, D-06120 Halle/Saale, Germany

Keywords: Cubic Zirconia, Fully Stabilized Zirconia, Plastic Deformation, Yield Stress, Work Hardening, Stress Relaxation, Activation Volume, Elastic Constants, Internal Friction, Dislocation, Line Tension, Precipitation Hardening, Peierls Stress, Recovery

Abstract

Fully stabilized (cubic) zirconia has a relatively high yield stress up to temperatures of about 1400 °C. Therefore and owing to its chemical stability it may be a constituent of future high-temperature structural materials. Cubic zirconia deforms by the glide of dislocations of 1/2⟨110⟩ Burgers vectors. The most prominent slip plane is of the type {001}, but {111} and {110} planes may also be activated. Three temperature ranges may be distinguished, differing in the macroscopic deformation behaviour and in the dislocation structures imaged by transmission electron microscopy. The high-temperature region above about 1250 °C is that most studied but not very well understood. Most probably the thermally activated character of the flow stress is controlled by recovery. Around 1150 °C, the flow stress is almost independent of the strain rate and temperature pointing at the action of athermal processes like long-range dislocation interactions controlling the flow stress. Below about 1000 °C, the plastic properties of cubic zirconia show the usual temperature and strain rate dependences, with both the flow stress and its strain rate sensitivity strongly increasing with decreasing temperature. These effects can be explained by the action of localized obstacles, and additionally by the Peierls mechanism below about 500 °C. Open problems are the different mechanisms controlling the dislocation mobility on non-cube slip planes, the nature of the localized obstacles, the transient effects at low and intermediate temperatures, the mechanism of the effect of the stabilizing yttria on the flow stress, and the role of recovery at high temperature.

1. Introduction

At a temperature of 1400 °C, fully stabilized (cubic) zirconia (c-ZrO_2, FSZ, or CSZ) has a relatively high yield stress of about 150 MPa, which together with a good chemical stability makes it an attractive constituent of high-temperature structural materials as, e.g., in multiphase ceramics or in the form of whiskers in ceramic matrix composites. The understanding of the behaviour of the zirconia components of these more complex microstructures requires the knowledge of the deformation parameters and mechanisms of cubic zirconia single crystals. c-ZrO_2 deforms by glide motions of dislocations. The respective slip geometry is described in Section 2. Yttria-stabilized crystals (Y-CSZ) were used for almost all experiments related to deformation properties so that this article is confined to these materials. The defect structure of calcia-stabilized crystals is described in [1, 2]. Detailed studies on the plastic properties of Y-CSZ have been performed by Heuer and coworkers [3 to 6] at or around a deformation temperature of 1400 °C. Recently, it was shown, however, that c-ZrO_2 can plastically be deformed down to 400 °C without confining hydrostatic pressure [7, 8]. Quite different mechanical parameters and deformation microstructures arise in the different temperature ranges. Accordingly, Section 3 on

the deformation parameters and Section 4 on the microstructures are divided according to the different temperature ranges. The results of supplementary experimental techniques such as *in situ* straining in the high-voltage electron microscope and measurements of dislocation velocities are described in Sections 5 and 6. Finally, the mechanisms controlling the plastic deformation and the open problems are being discussed in Section 7.

2. Slip Geometry

Fully stabilized zirconia is considered to have the cubic fluorite structure of the pure ZrO_2 high-temperature phase [9, 10]. The shortest Burgers vector in this structure is of the type 1/2 ⟨110⟩. Possible slip planes are the {001}, {110} and {111} planes. The core configurations of screw and edge dislocations on these planes are discussed in [11, 12], according to which the dislocations should not be dissociated. The straight dislocations are electrically neutral except the edge dislocation on the {100} plane, which may be either positively or negatively charged. A dislocation of zero net charge may then be composed of short segments of opposite charge divided by half-jogs.

The slip plane of the lowest glide resistance is the {001} plane (see, e.g., [13, 6] and Section 4), the reason of which cannot easily be understood within the framework of the dislocation energies or a simple Peierls model. It should be connected with the core structures of the intermediate configurations [14]. The plastic properties of cubic zirconia were mostly studied under compression at an orientation for single slip on a {001} plane, i.e. with a ⟨112⟩ compression axis, as depicted in Fig. 1. This orientation may be called a "soft" orientation for cube slip. The

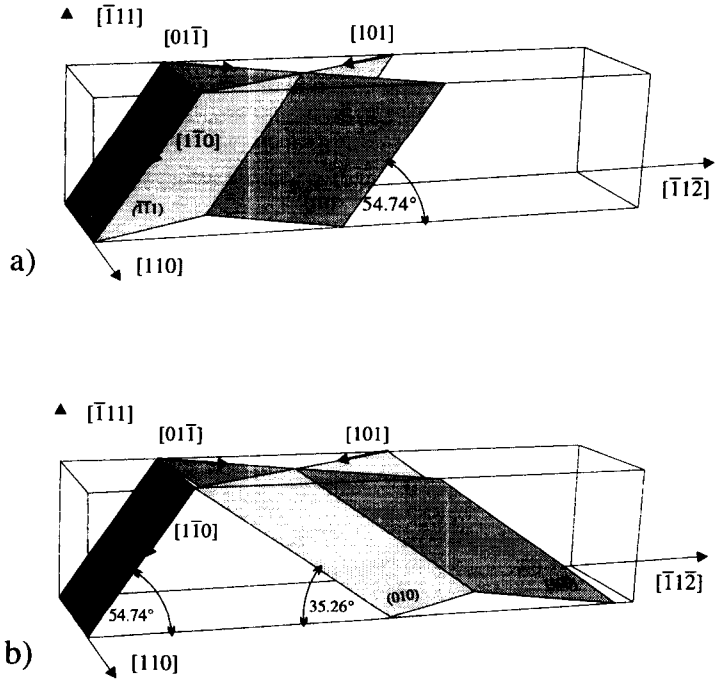

Fig. 1 Slip geometry for the single slip orientation with a [$\bar{1}$1$\bar{2}$] compression axis

Table 1

Orientation factors for deformation of c-ZrO_2 along $[\bar{1}\,1\,\bar{2}]$ and [100]

plane	Burgers vectors; orientation factors for $[\bar{1}\,1\,\bar{2}]$, orient. factors for [100]					
(001)	$[1\,\bar{1}\,0]$; 0.47,	0	[110]; 0,	0		
(100)	$[0\,1\,\bar{1}]$; 0.35,	0	[011]; 0.12,	0		
(010)	[101]; 0.35,	0	$[10\bar{1}]$; 0.12,	0		
(111)	$[0\,1\,\bar{1}]$; 0.41,	0	$[1\,\bar{1}\,0]$; 0.27,	0.41	$[10\bar{1}]$; 0.14,	0.41
$(11\bar{1})$	[101]; 0.41,	0.41	$[1\,\bar{1}\,0]$; 0.27,	0.41	[011]; 0.14,	0
$(1\bar{1}\,1)$	$[10\bar{1}]$; 0.27,	0.41	[011]; 0.27,	0	[110]; 0,	0.41
$(\bar{1}\,11)$	[110]; 0,	0.41	[101]; 0,	0.41	$[0\,1\,\bar{1}]$; 0,	0
(101)	$[10\bar{1}]$; 0.25,	0.5				
$(10\bar{1})$	[101]; 0.25,	0.5				
(011)	$[0\,1\,\bar{1}]$; 0.25,	0				
$(01\bar{1})$	[011]; 0.25,	0				
(110)	$[1\,\bar{1}\,0]$; 0,	0.5				
$(1\bar{1}\,0)$	[110]; 0,	0.5				

corresponding orientation factors of the relevant slip systems are listed in Table 1 together with those for the ⟨100⟩ orientation of the compression axis, in which the orientation factors of cube slip are zero. The major part of the experimental data of Sections 3 and 4 refer to the "soft" single slip orientation. Other orientations of the compression axis, which favour slip on planes other than cube planes, are discussed in Sections 3.4 and 4.4.

Recently, the fluorite structure of Y-CSZ has been questioned at temperatures below about 800 °C. Electron diffraction patterns show {odd, odd, even} reflections, which are forbidden in the ideal fluorite structure ([15] and several others). A convergent-beam electron diffraction study [16] revealed a space group $P\bar{4}3m$, which is different from that of the fluorite structure $Fm\bar{3}m$ and the known tetragonal structure $P4_2/nmc$. The new structure results from the fluorite structure by displacing the oxygen ions in {111} directions. The lattice would then be primitive cubic with the shortest Burgers vector of type ⟨100⟩. Electron microscopy contrast extinction analysis of dislocations produced during deformation between 500 °C and 700 °C [7, 8] as well as deformation experiments under confining hydrostatic pressure down to 250 °C [17, 18], however, have shown that all dislocations have Burgers vectors in ⟨110⟩ directions. Preliminary experiments for determining the magnitude of the Burgers vectors by convergent-beam electron diffraction are consistent with the usual 1/2 ⟨110⟩ Burgers vectors [19]. This open problem needs further investigation.

3. Macroscopic Deformation Data of Yttria Fully-Stabilized Zirconia

As described above, Sections 3 and 4 will concentrate on yttria fully stabilized zirconia single crystals deformed in compression in a $[\bar{1}\,1\,\bar{2}]$ direction to initiate single slip on $(001)[1\,\bar{1}\,0]$. Three different temperature ranges are being distinguished.

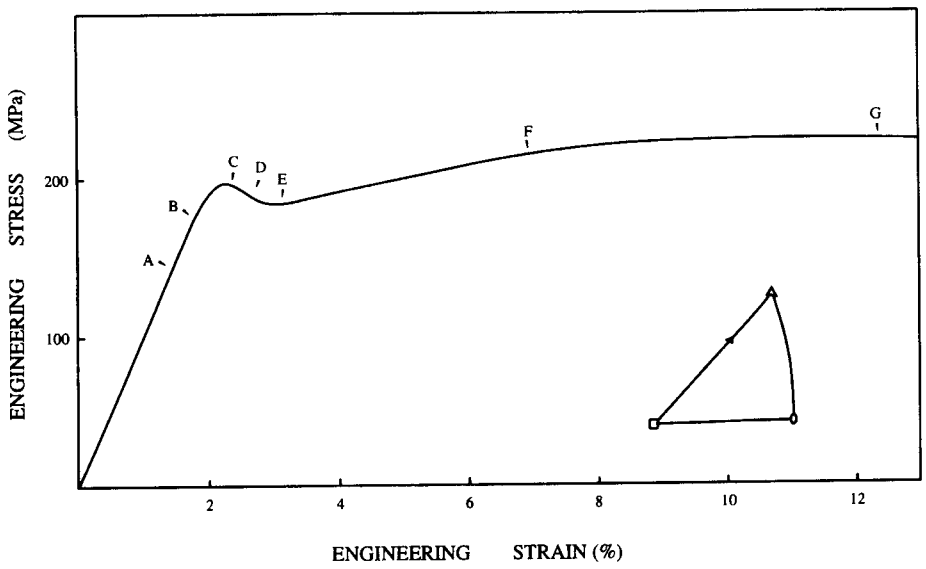

Fig. 2 Stress-strain curve of ZrO_2-9.4mol%Y_2O_3 at 1400 °C and $\dot{\varepsilon} = 1.3*10^{-5}$ s^{-1} (After [3])

3.1. High-Temperature Range

This temperature range above about 1250 °C is being most intensively investigated. Many of the experiments have been performed at a standard temperature of 1400 °C. Figure 2 shows a deformation curve typical of a crystal of a nominal yttria concentration of 9.4 mol% and a low strain rate. Many deformation curves, especially at low strain rates, exhibit the characteristic yield drop effect with an upper and a lower yield point. In this case, the upper yield point is taken as the yield stress σ_y. After the lower yield point the work-hardening rate decreases from near 1000 MPa to a very low value. Stress relaxation or partial unloading experiments show that a very substantial part of the flow stress relaxes [20]. The stress-strain curves are usually smooth, but if the flow stress exceeds about 300 MPa serrated flow will occur [21]. After this work, serrations appear irrespective of whether the increase of the flow stress is accomplished by an increased yttria concentration, a lower temperature, or a higher strain rate.

The yield stress of cubic zirconia depends on the concentration of the stabilizing yttria [21 to 23] as outlined in Fig. 3, where the yield stress is plotted as a function of the nominal yttria concentration which had been quoted by the supplier of the crystals (Ceres Corp., Waltham, MA). Different EDX measurements of some of the materials yielded concentrations about 2 mol% higher than the nominal ones. The flow stress increases with increasing yttria concentration reaching a maximum at about 20 mol%.

The temperature dependence of the flow stress was measured at constant strain rates [5, 13, 24] and under creep conditions [25 to 27]. Figure 4 shows that, at constant strain rate, the yield stress of the material having a nominal yttria concentration of 9.4 mol% decreases linearly with increasing temperature up to 1500 °C. Apparent activation energies Q_e were deduced from Arrhenius plots of the logarithm of the strain rate $\dot{\varepsilon}$ and from temperature change experiments according to

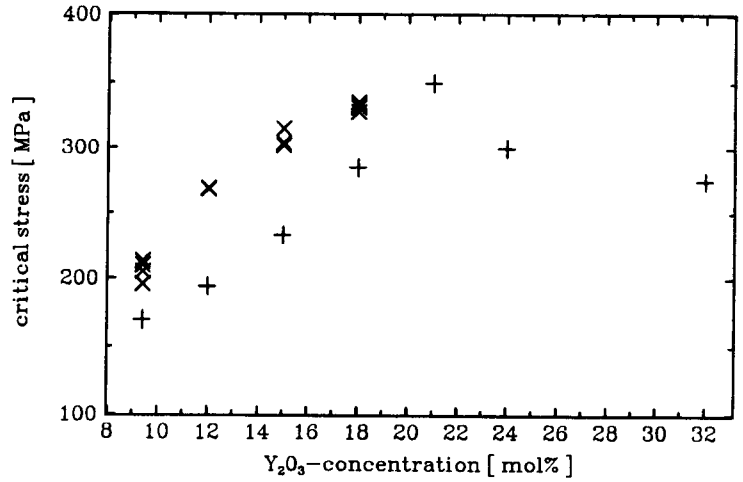

Fig. 3 Dependence of critical flow stress at 1400 °C on yttria concentration. Data at a strain rate of $\dot{\varepsilon} = 1.2*10^{-5}$ s^{-1} from [21], of $\dot{\varepsilon} = 1.2*10^{-4}$ s^{-1} from [23]

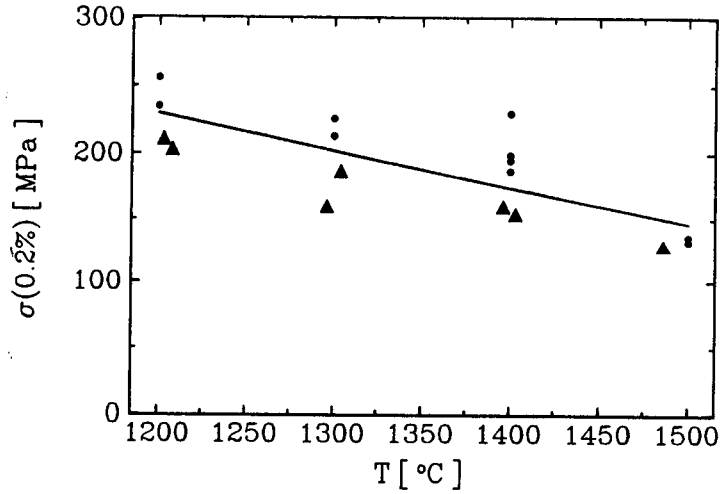

Fig. 4 Temperature dependence of 0.2% proof stress of ZrO_2-9.4mol%Y_2O_3 in the high-temperature region (After [5])

$$Q_e = - k T^2 (d \ln \dot{\varepsilon} / d T)_\sigma \qquad (1)$$

For the Arrhenius plots, the strain rates were normalized to the condition of constant stress σ. Creep data for temperatures up to 1800 °C exhibit two temperature ranges for crystals with 9.4 and 21 mol% yttria with different activation energies as the Arrhenius plots of Fig. 5 and Table 2 indicate. The activation energies were lower in the higher temperature range.

The dependence of the flow stress σ on the strain rate $\dot{\varepsilon}$ is conveniently expressed by the so-called strain rate sensitivity I with

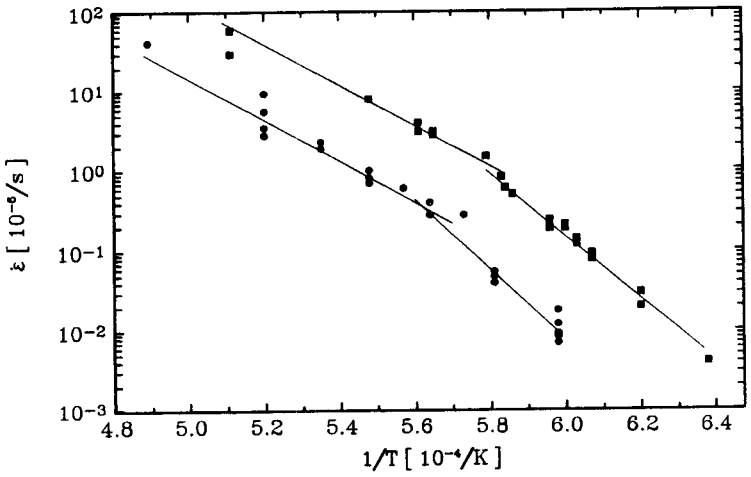

Fig. 5 Arrhenius plots of high-temperature creep data. Upper curve 9.4mol% Y_2O_3, lower curve 21 mol% Y_2O_3 (After [27])

Table 2

Creep parameters of cubic zirconia

yttria conc. and method	temp. range	stress exponent m*	act. energy Q_e [eV]
9.4 mol% Arrhenius-plot			
Ref. [26]	1300 °C - 1400 °C	7.3 ± 0.5	7.4 ± 0.3
Ref. [27]	1300 °C - 1450 °C		7.5
9.4 mol% Arrhenius-plot			
Ref. [26]	1450 °C - 1550 °C	4.5 ± 0.4	6.1 ± 0.3
Ref. [27]	1450 °C - 1750 °C		5.5
21 mol% Arrhenius-plot			
Ref. [27]	1400 °C - 1500 °C		8.9 ± 0.6
temp.-change			
Ref. [27]	1400 °C - 1500 °C	5.4 ± 0.4	8 ± 1
21 mol% Arrhenius-plot			
Ref. [27]	1500 °C - 1800 °C		5.6 ± 0.4
temp.-change			
Ref. [27]	1500 °C - 1800 °C	2.9 ± 0.2	5.8 ± 0.5

$$I = (d\sigma / d \ln \dot{\varepsilon})_T \quad (2)$$

or by the stress exponent m* with

$$m^* = (d \ln \dot{\varepsilon} / d \ln \sigma)_T \quad (3)$$

Using Eq. 2 changes Eq. 1 into

$$Q_e = - k T^2 (d\sigma/dT)_{\dot{\varepsilon}} / I \quad (4)$$

In the early papers, the strain rate sensitivity of the flow stress had not been investigated systematically in constant strain rate tests. Figure 3 displays measurements of the yield stress of different materials deformed at 1400 °C at two basic strain rates, viz. $1.2*10^{-5}$ s^{-1} and $1.2*10^{-4}$ s^{-1}. Table 2 lists also stress exponents that are calculated from load change experiments during creep by using Eq. 3. They decrease with increasing temperature.

In order to study the strain rate sensitivity of the flow stress in more detail, strain rate cycling (SRC) and stress relaxation experiments (R) were performed at 1400 °C [23, 20, 28]. As originally shown in [23], if plotted as ln ($-\dot{\sigma}$) versus σ like in Fig. 6 the relaxation curves reveal an unusual strain rate sensitivity. Since the negative stress rate $-\dot{\sigma}$ in the relaxation experiment is proportional to the instantaneous strain rate, the inverse slope of the curve equals the strain rate sensitivity I of Eq. 2. Thus, for the microstructure of the actual plastic strain the relaxation curve describes the dependence of I over a certain range of strain rate or stress. Single values of I quoted in this paper mostly refer to the beginning of the relaxation test, i.e. to the strain rate before the relaxation. At 1400 °C, particularly at small strains and high strain rates (which corresponds to high stresses at the instantaneous microstructure), the relaxation curve starts with a very low strain rate sensitivity I of the flow stress. At a certain value of stress, or strain rate, the relaxation curve abruptly changes to much higher values of I, which decrease with further

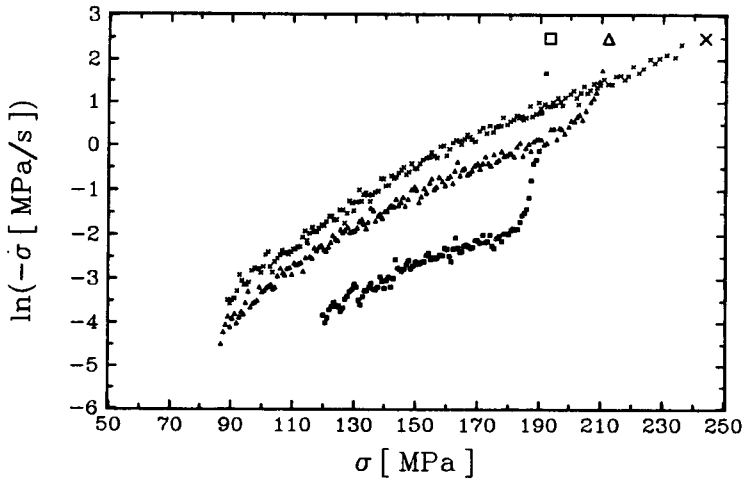

Fig. 6 Stress relaxation curves of ZrO_2-9.4mol%Y_2O_3 at 1400 °C and a strain rate of 10^{-4} s^{-1}. Thre relaxation curves at increasing strain (After [20])

decreasing stress. This "inverse" dependence of I on the strain rate was confirmed by strain rate cycling experiments at different basic strain rates. At larger strains, the initial region of low strain rate sensitivity gradually disappears. Most experiments, except those in [23, 20, 28], were performed at low strain rates, not involving the above effect. The respective strain rate sensitivities, including the m* values of Table 2, do not correspond to the initial range of low values of I.

In the high-temperature range, the flow stress of cubic zirconia depends on the concentration of the stabilizing yttria and on the temperature. The strain rate sensitivity shows an "inverse" dependence on the basic strain rate (or the instantaneous stress). The discussion in Section 7 will show that these observations can be explained by a strong influence of diffusion-controlled recovery on the dislocation behaviour.

3.2 Intermediate Temperature Range

Except the early study published in [29], which proved plastic deformation of cubic zirconia at 1150 °C and 700 °C without additional confining hydrostatic pressure, all the other straining experiments were performed at or above 1200 °C so that this material was considered brittle at lower temperatures. Recently, plastic deformation of ZrO_2-9.4mol%Y_2O_3 was achieved in air at a low strain rate of 10^{-6} s^{-1} down to 400 °C [7, 8, 30]. Typical stress-strain curves are demonstrated in Fig. 7. In all experiments, similar sequences of strain rate cycling (SRC) and

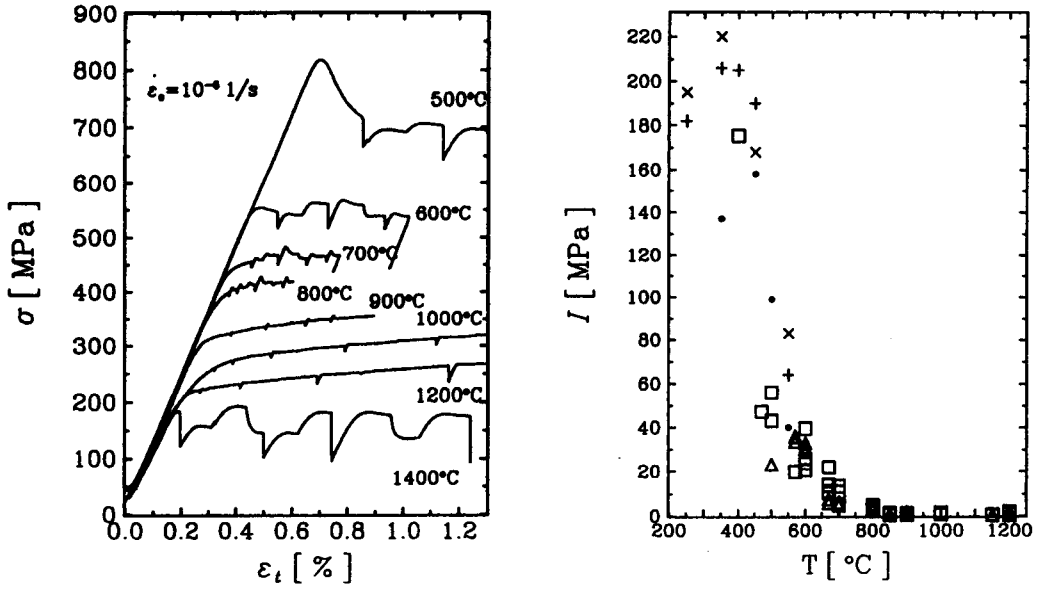

Fig. 7 Stress-strain curves of ZrO_2-9.4mol%Y_2O_3 at different temperatures. After [28, 7]

Fig. 8 Dependence of the strain rate sensitivity I of c-ZrO_2 on temperature.
Low-temperature data under confining hydrostatic pressure from [17, 18], $\dot{\varepsilon}$ = 2*10^{-4} s^{-1}:
+ R 9.4mol%Y_2O_3, × R 12.6mol%Y_2O_3, • R 14.9mol%CaO;
Other data from [28, 7], $\dot{\varepsilon}$ = 10^{-6} s^{-1}: □ R 9.4mol%Y_2O_3, Δ SRC 9.4mol%Y_2O_3

stress relaxation tests (R) were carried out in the course of deformation. In Fig. 8, the strain rate sensitivities I derived from these experiments are plotted as a function of temperature. The deformation curve at 1150 °C already qualitatively reveals that the flow stress is almost insensitive to the strain rate at this temperature. The flow stress shows very little relaxation for relaxation times in the order of 30 min. In Fig. 8, the value of I close to zero corresponds to high values of m* (100 or larger).

Figure 9 is a plot of the temperature sensitivity of the flow stress $-\Delta\sigma/\Delta T$, measured in temperature change experiments, against the temperature. This quantity, too, has got a low value at 1150 °C.

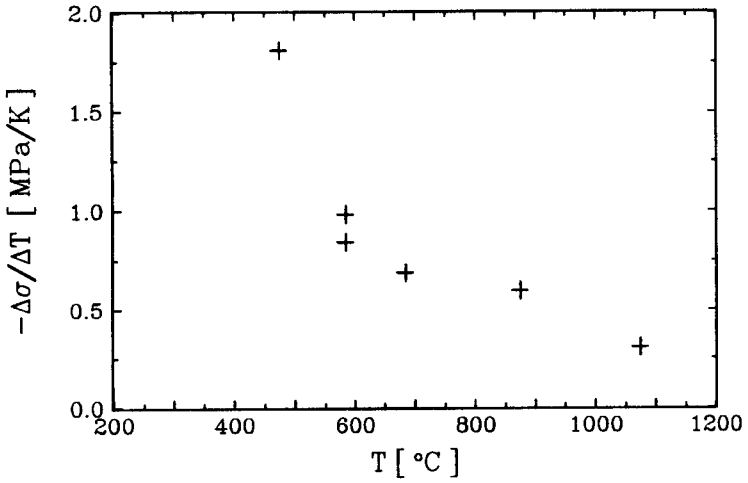

Fig. 9 Dependence of the temperature sensitivity of the flow stress $-\Delta\sigma/\Delta T$ of ZrO_2-9.4mol%Y_2O_3 on the temperature. Data from [28, 7]

Thus, it follows that the flow stress around 1150 °C is almost insensitive to strain rate and temperature, which in Section 7 will be explained by the athermal motion of dislocations.

3.3 Low-Temperature Range

As Fig. 7 shows, macroscopic plastic deformation of cubic zirconia with a well-defined yield stress was successfully performed at atmospheric pressure down to 500 °C [7, 8]. Specimens deformed at 400 °C showed clear deviations from the elastic line and proved plastic deformation in stress relaxation experiments. They broke, however, shortly after a macroscopic yield point had formed. Although the stress at the yield point may have been influenced by the previous relaxation tests, in Fig. 10 it is included in the temperature dependence of the yield stress. The lowest temperature at which macroscopic plastic deformation has been achieved is 250 °C in compression experiments under confining hydrostatic pressure, which prevents brittle fracture at the high flow stress [17, 18, 31]. The data of these experiments on three different materials are also plotted in Fig. 10. In comparing both data sets, one should consider the different sources of the crystals and different strain rates. In general, a strong increase of the yield stress is observed at decreasing temperature. The temperature sensitivity of the flow stress $-\Delta\sigma/\Delta T$ can be deduced from Fig. 7. It can also be measured by temperature change experiments as demonstrated in Fig.

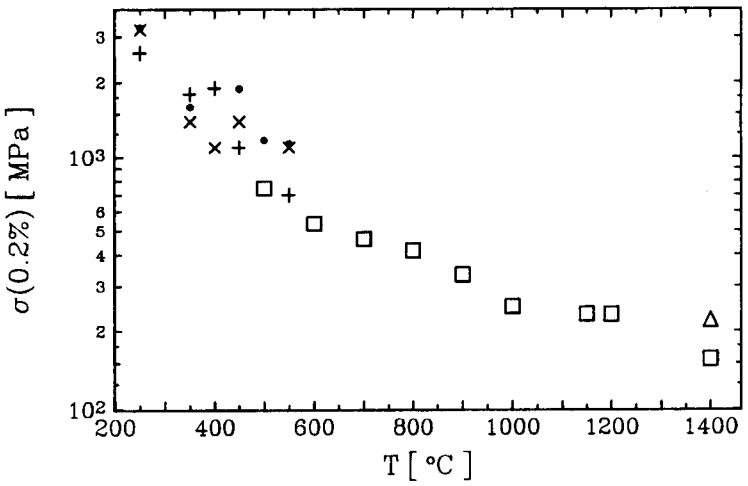

Fig. 10 Temperature dependence of the 0.2 % proof stress $\sigma_{0.2}$ of ZrO_2-9.4mol%Y_2O_3. Low-temperature data under confining hydrostatic pressure including two other materials from [17, 18]; other data from [28, 7]. Symbols as in Fig. 8

9. Both methods agree above about 800 °C. At lower temperatures, the values from temperature cycling tests are lower than those from the flow stress versus temperature curve.

The flow stresses of the three materials measured under hydrostatic pressure all exhibit a weak maximum at or slightly above 400 °C, superimposed on the continuous increase at decreasing temperatures. Although these maxima are within the scattering of the experimental data they seem to represent a real effect.

In Fig. 8, the strain rate sensitivity of the flow stress I measured by strain rate cycling and stress relaxation experiments is plotted as a function of temperature. This figure again comprises the measurements at atmospheric pressure and under additional hydrostatic pressure. Together with the flow stress increase, the strain rate sensitivity strongly increases at decreasing temperature. At the very lowest temperatures, however, the curves of the different materials seem to reach constant values.

As mentioned above, the stress relaxation curves describe the strain rate sensitivity over a range of strain rate or stress. The curves plotted in Fig. 11, covering almost the whole temperature range, exhibit different shapes at different temperatures and strains, emphasizing the classification into the different temperature ranges. "Normal" bending of the curves towards the stress axis occurs at high temperatures and in the middle of the low-temperature range. At very low temperature (400 °C), I depends only weakly on the stress.

At 500 °C, after strain rate changes the stress-strain curves show a smooth transition from the stress level corresponding to the original strain rate to that of the new one, without yield drop effects (see Fig. 7). At the transition between the athermal behaviour around 1150 °C and the real low-temperature behaviour, the strain rate changes are accompanied with yield drop effects, well pronounced at 700 °C and 800 °C. Similar yield drop effects appear also after stress relaxation and after partial unloading. Figure 12 demonstrates the dependence of the transient

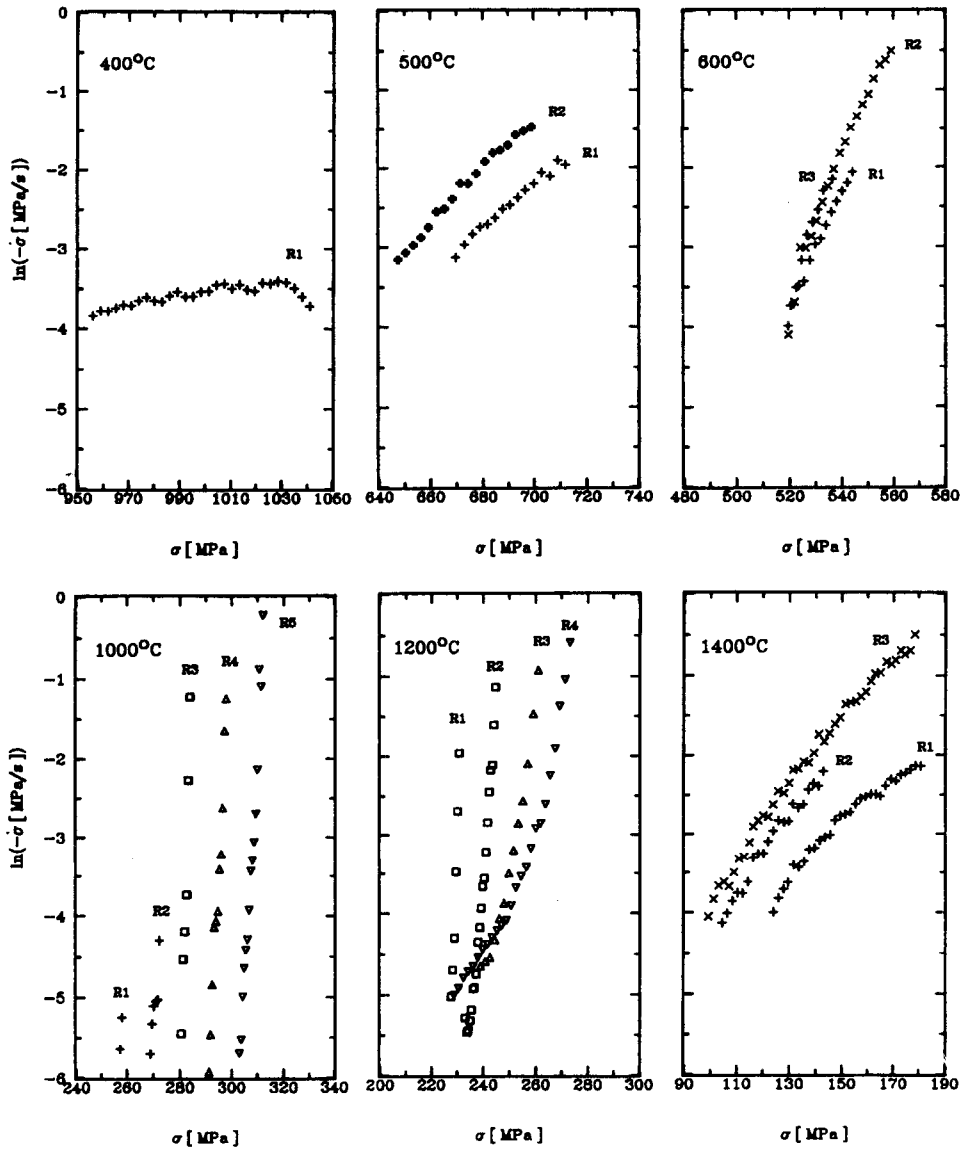

Fig. 11 Stress relaxation curves of ZrO_2-9.4mol%Y_2O_3 at a strain of about 0.5 % at different temperatures. A strain rate of $\dot{\varepsilon} = 10^{-6}\ s^{-1}$ corresponds to ln (- $\dot{\sigma}$ [MPa]) ≅ -2. Data from [28]

stress increments owing to partial unloading on the ageing time. They seem to reach a saturation value. In creep experiments transient phenomena also appear after load changes. As plotted in Fig. 13, after a small load increment the strain rate first increases before it slowly drops back to almost the value before the load increment.

In conclusion one can say that between about 800 °C and 250 °C cubic zirconia shows the usual low-temperature deformation behaviour with strongly increasing flow stress and its strain rate

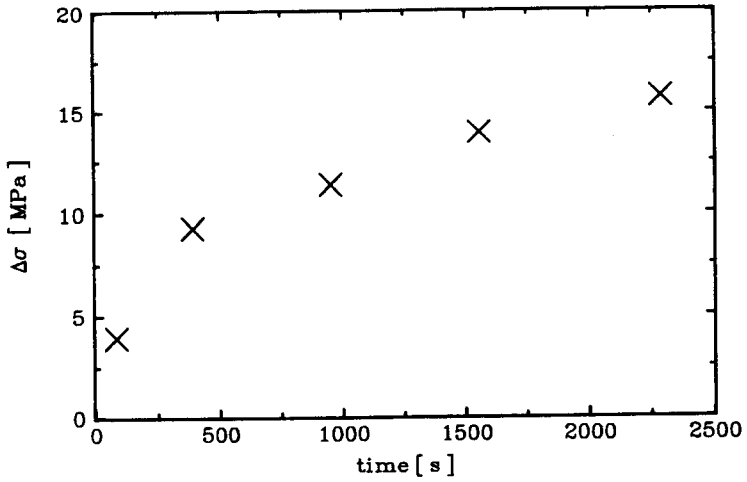

Fig. 12 Stress increment at yield point effect after partial unloading of ZrO_2-9.4mol%Y_2O_3 as a function of ageing time at 685 °C (After [7])

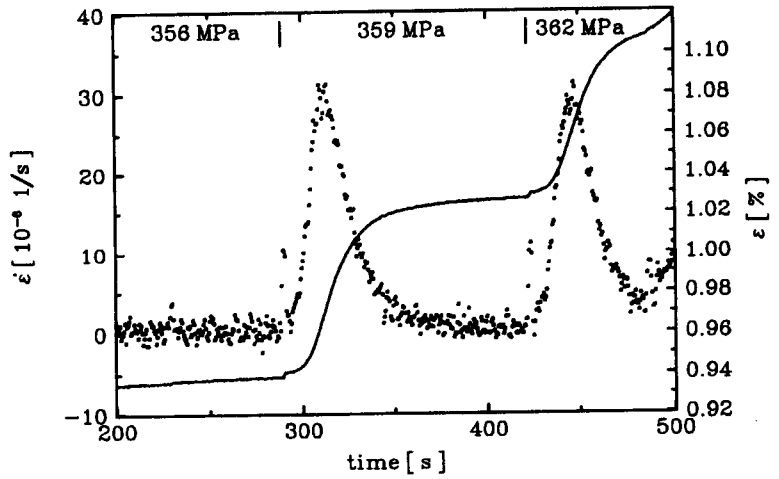

Fig. 13 Time dependence of the strain (line) and of the strain rate (dots) during load change experiments on ZrO_2-9.4mol%Y_2O_3 at 900 °C (After [7])

sensitivity at decreasing temperature. Perhaps, the strain rate sensitivity slightly decreases again below about 400 °C. Between about 600 °C and 1000 °C transient effects are associated with changes of the deformation parameters.

3.4 Orientation Dependence of the Flow Stress

In order to differentiate between the activation of the different possible slip systems, a few deformation experiments [13, 6, 20, 28] have been carried out in the high-temperature region with compression axes different from the $[\bar{1}1\bar{2}]$ axis described in Sections 3.1 to 3.3 favouring single slip on a {001} plane. With a ⟨100⟩ compression axis, slip on {001} planes should be

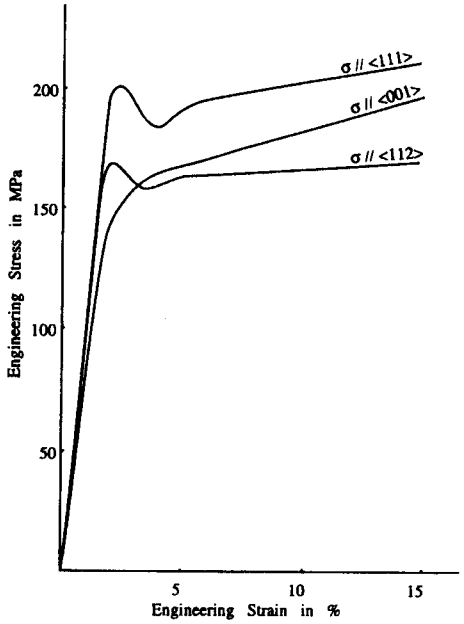

Fig. 14 Stress-strain curves of deformation of ZrO_2-9.4mol% Y_2O_3 at 1400 °C at three different orientations of the compression axis (After [13])

completely suppressed. Figure 14 shows stress-strain curves from Ref. [13] for compression axes in ⟨100⟩, ⟨111⟩ orientations and the usual ⟨112⟩ one at a strain rate of 10^{-5} s^{-1}. There is almost no difference in the yield stress between compression in ⟨100⟩ and ⟨112⟩ directions. At 1500 °C, the differences completely disappear [13]. Greater differences than those at 1400 °C arise at lower temperatures (1200 °C) [13] and higher strain rates (10^{-4} s^{-1} in [20, 28]). At 1150 °C, the yield stress in ⟨100⟩ direction is about twice that in ⟨112⟩ direction [28]. The main effect in Fig. 14 seems to be that the characteristic yield drop effect disappears for the ⟨100⟩ compression axis. This is at variance with the experiments in [20, 28], where pronounced yield drops were observed for compression in ⟨100⟩ at strain rates of 10^{-6} and 10^{-4} s^{-1}. The strain rate sensitivity for compression in ⟨100⟩ amounts to I ≅ 40 MPa, independent of the strain rate [18, 26] so that it is slighly larger than that of deformation in ⟨112⟩ at low strain rate (10^{-6} s^{-1}). "Inverse" bending of the stress relaxation curves connected with very low values of I occurring at the beginning of deformation in ⟨112⟩ at high strain rates is missing at the ⟨100⟩ compression axis. The experimental activation energy does not seem to depend on the specimen orientation [13]. Tests were performed in ⟨115⟩, ⟨113⟩ and ⟨029⟩ orientations with different ratios between the orientation factors for {001}, {110} and {111} slip have also been performed [6]. Flow stress data, however, are not given.

4. Microstructure of Deformed Yttria Fully Stabilized Zirconia Crystals

This Section discusses the information available about the active slip systems and the arrangements of dislocations obtained by optical microscopy and X-ray topography but mainly by conventional transmission electron microscopy (TEM). It is arranged in the same way as Section 3, i.e. Sections 4.1 to 4.3 correspond the $[\bar{1}\,1\,\bar{2}]$ compression axis for single slip on $(001)[1\,\bar{1}\,0]$.

4.1 High-Temperature Range

The first problem of describing the microprocesses of deformation is in the determination of the active slip systems and their specific resolved critical stresses. Macroscopic information on this topic can be obtained by optical methods like etch pit patterns, slip step observations on the surface, and optical birefringence. Etch pits at dislocations can be produced by etching the {111} or {100} faces with KOH at 500 °C for 15 min [3, 32]. Other surfaces have not successfully been etched. At the beginning of deformation up to about stage D in Fig. 2, single slip on (001)[1$\bar{1}$0] dominates during the deformation along [$\bar{1}$1$\bar{2}$], which was revealed from slip steps and etch pit traces in [110] direction on the ($\bar{1}$11) surface and from slip bands in [1$\bar{1}$0] direction visible in birefringence on the (110) side face according to the scheme of Fig. 1 [3].

After the lower yield point additional traces of etch pits appear in the ⟨110⟩ directions on the ($\bar{1}$11) face as well as slip steps in [1$\bar{1}$0] direction on the (110) side face. This is consistent with the activation of secondary slip on {111} planes with Burgers vectors out of the (001) plane [3]. As will be described below, careful stereographic analysis of TEM micrographs proved secondary slip on other planes of {100} type [20, 28].

TEM work at 1400 °C confirms the (001) plane as the primary slip plane for deformation along [$\bar{1}$1$\bar{2}$]. Figure 15 shows a micrograph from [4], which represents the typical dislocation structure at small strains, which is characterized by a single set of dislocations with 1/2 [1$\bar{1}$0] Burgers vectors according to the notation in Fig. 1. The dislocations are smoothly bent, sometimes showing segments in preferred orientations connected by others of large curvature. The dislocations have jogs trailing dislocation dipoles. Frequently, the dipoles are pinched-off into small dislocation loops.

As mentioned above, secondary slip is activated at larger strains. In Fig. 16, primary dislocations are labelled by p and secondary ones by s. The secondary dislocations have 1/2 [01$\bar{1}$] and 1/2 [101] Burgers vectors. Sometimes they form nodes, indicated by N. The formation of junctions according to the reaction

$$1/2\,[1\bar{1}0] + 1/2\,[01\bar{1}] = 1/2\,[10\bar{1}] \qquad (5)$$

is accompanied by a gain in energy. The density of the junctions is not very high. At small strains the distance between them (the link length of dislocation segements) is larger than 2 to 3 μm. Finally, all Burgers vectors possible of type 1/2 ⟨110⟩ are present with fractions between 25 and 11 % [4]. The whole dislocation structure is quite homogeneous. At 1400 °C, the total dislocation density increases from $0.9*10^{12}$ m^{-2} at stage B of Fig. 2 up to $4.5*10^{12}$ m^{-2} at stages F and G [4]. As will be discussed in Section 7.2, these densities are very low in terms of long-range dislocation interactions as a mechanism controlling the flow stress. Similar dislocation structures were observed over the whole high-temperature range (e.g. [5, 22, 24 to 26]) so that they will not be discussed here in more detail.

Probably all or most of the dislocation structures mentioned so far are imaged after the deformed specimens were unloaded and slowly cooled down. In [4], cooling from 1400 °C down to 1000 °C was performed within 15 min, and it is argued that this should be fast enough to avoid substantial recovery during cooling. A note in [5] says that some recovery might occur during the standard procedure but that quenched specimens did not show a different shape or density of

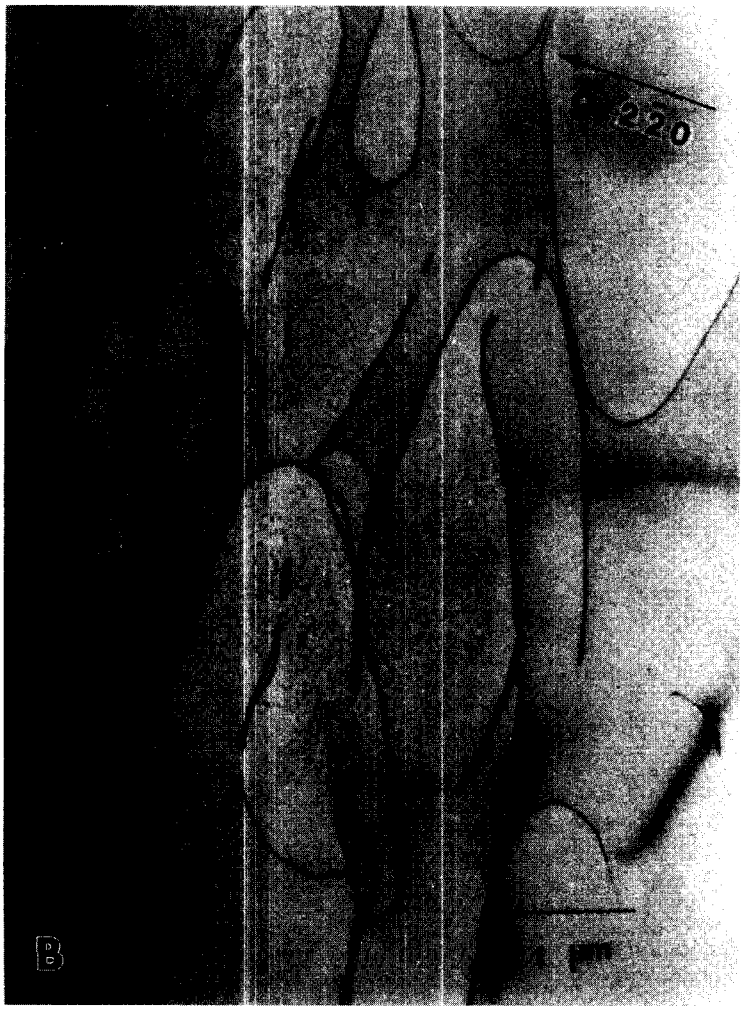

Fig. 15 Dislocations on the primary (001) plane after compression of ZrO_2-9.4mol%Y_2O_3 in $[\bar{1}1\bar{2}]$ direction at 1400 °C up to stage B in Fig. 2. (001) foil plane (After [4])
By courtesy of Taylor & Francis

dislocation debris (not of dislocations in general). The pinched-off shape of dislocation dipoles, however, indicates diffusion-controlled (climb) processes to be active at the standard deformation temperature of 1400 °C. In order to obtain more information on this problem, special experiments were performed to compare the dislocation structures produced in the specimens of a nominal yttria concentration of 9.4 mole % by deformation at 1400 °C after cooling without load, as in the standard procedure, and under full load [20, 28]. As the flow stress increases rapidly with decreasing temperature, the dislocation glide activity should quickly freeze during cooling with the dislocation structure being closer to that under deformation conditions. Cooling under load, however, does not generally prevent diffusion-controlled recovery. Nevertheless, as Fig. 17 shows, the shape of dislocations differs between both treatments and the dislocation

Fig. 16 Dislocation structure in ZrO_2-9.4mol%Y_2O_3 at larger strain (stage G in Fig. 2) at 1400 °C showing dislocations of primary and secondary Burgers vectors. (001) foil plane (After [4]) By courtesy of Taylor & Francis

density is remarkably higher after cooling under load (at 2.5 % strain, the density of primary dislocations is $1.6*10^{13}$ m^{-2} and of secondary ones it is $0.5*10^{13}$ m^{-2}, compared to $2.6*10^{12}$ and $0.2*10^{12}$ m^{-2} in the unloaded specimens at 3 % strain). These densities are about a factor of five higher than those determined after the standard treatment by TEM (about $3*10^{12}$ m^{-2} at about 2.5 % strain [4]) or by replica electron microscopy of etched surfaces ($4.6*10^{12}$ m^{-2} at 1.1 % strain [23]). From these observations it is concluded that probably all dislocation structures of high-temperature deformation discussed in the literature so far are severely influenced by recovery and that the respective dislocation densities do not correspond to the dislocation structure under the deformation conditions. As it will be discussed in Section 7.2, recovery may be the mechanism controlling the thermally activated processes during the deformation of fully stabilized zirconia in the high-temperature range.

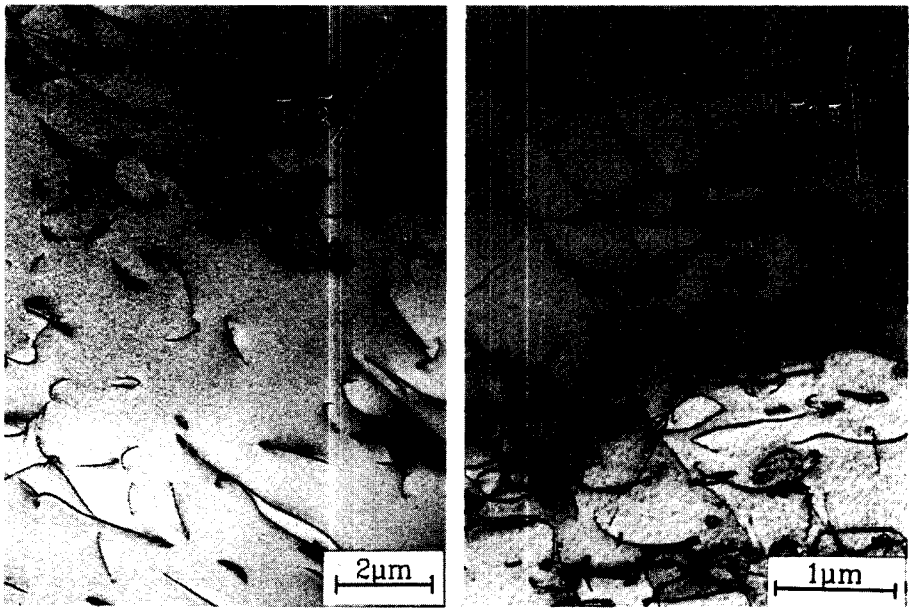

Fig. 17 Comparison between dislocation structures in ZrO_2-9.4mol%Y_2O_3 produced by plastic deformation of about 2.5 % in $[\bar{1}\,1\,\bar{2}]$ direction at 1400 °C. $(\bar{1}\,11)$ foil plane. a) after cooling without load. b) after cooling under load. Note the different magnifications in a) and b)

TEM can also help determine the type of slip planes activated as secondary slip in the "soft" orientations for cube slip as the $[\bar{1}\,1\,\bar{2}]$ compression axis. As described above, optical methods showed slip on {111} planes as secondary slip [3]. However, the corresponding evidence by TEM in [3] is not very strong. During recent TEM tilting experiments micrographs were taken at or near zone axes where possible slip planes are imaged edge-on [20]. Part of the result is shown in Fig. 18, using the notation of Fig. 1 and demonstrating that the secondary dislocations appear most straight in the image near the $[00\bar{1}]$ pole in directions corresponding to {001} (secondary) slip planes, imaged edge-on (Fig. 18c). Their bowed-out structure is well visible in the image at the $[1\,\bar{1}\,0]$ pole with the possible {111} (secondary) planes edge-on (Fig. 18d). This proves {001} planes as the secondary slip planes in the "soft" orientation for cube slip. The images are also not consistent with {110} (secondary) planes. The result can well be understood if one considers that the orientation factor of 0.35 for the {001} secondary planes (see Table 1) is not much smaller than that of 0.41 for {111}slip but that the critical flow stress on {111} is probably about 30 % higher, as will be discussed in Section 4.4.

Thus, the high-temperature deformation of Y-FSZ in "soft" orientations for cube slip is carried by glide on cube planes. At the beginning of deformation, single (primary) slip dominates on the system of the highest orientation factor. Later on, further (secondary) cube planes are activated. In specimens slowly cooled down to room temperature, recovery most probably prevents the dislocation structures and densities characteristic of the deformation process at high temperatures to be observed by TEM.

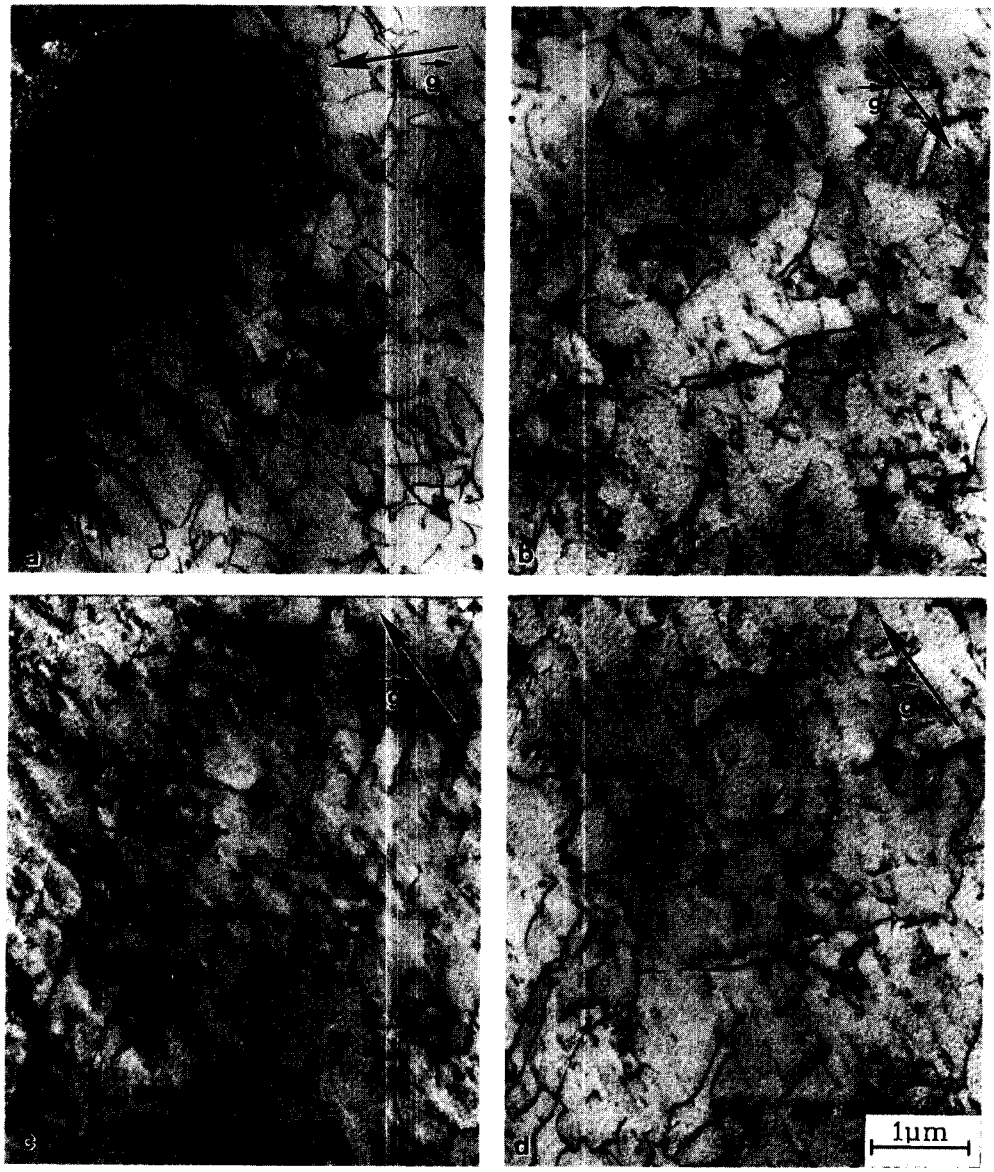

Fig. 18 Determination of the plane of secondary slip in ZrO_2-9.4mol%Y_2O_3 deformed at 1400 °C in $[\bar{1}\,1\,\bar{2}]$ direction, cooled under load

a) $[1\,\bar{1}\,\bar{1}]$ pole and $\vec{g}$ vector for imaging almost all dislocations

b) $[1\,\bar{1}\,\bar{1}]$ pole and $\vec{g}$ vector with only secondary dislocations being imaged

c) near the $[00\bar{1}]$ pole and $\vec{g}$ vector for imaging only secondary dislocations. {100} planes for the secondary dislocations are imaged nearly edge-on

d) $[1\,\bar{1}\,0]$ pole and $\vec{g}$ vector for imaging only secondary dislocations. {111} planes for the secondary dislocations are imaged edge-on

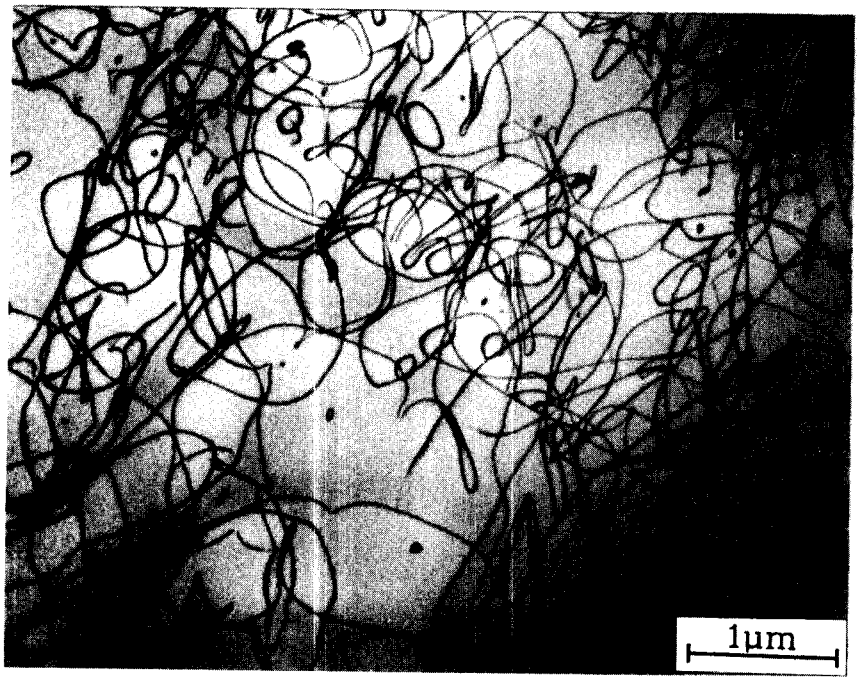

Fig. 19 Dislocation structure after deformation of 1.4 % in $[\bar{1}\,1\,\bar{2}]$ direction at 1200 °C, cooled under load. (001) foil parallel to the primary slip plane.

4.2 Intermediate Temperature Range

Slip steps on the surface and birefringence patterns in the optical microscope prove that up to the maximum strain of 1.6 % studied until now only the $(001)[1\,\bar{1}\,0]$ primary slip system is activated [7, 28]. Figure 19 presents a typical example of the dislocation structure with the dislocations still in a relatively homogeneous distribution. They are preferentially oriented in screw, edge and cube directions. There are a number of large jogs produced by cross slip. Stereo pairs reveal that the dislocations are not arranged solely on cube planes and that the cross slip planes probably are the {111} planes. There exists a relatively large number of dislocation loops, mostly on the primary slip plane, occasionally, however, also on other planes. The dislocation density in specimens cooled under load is of the same order of magnitude as that at 1400 °C, i.e. about $2*10^{13}$ m^{-2}. *In situ* straining experiments in a high-voltage electron microscope yielded additional information on the dislocation behaviour in this temperature range, which will be described in Section 5.

4.3 Low-Temperature Range

After deformation along $[\bar{1}\,1\,\bar{2}]$, only dislocations of the primary $(001)[1\,\bar{1}\,0]$ slip system have been observed so far [7, 8, 28]. As Fig. 20a shows for 700 °C, the dislocations are of curly shape, even in the unloaded state, indicating that dislocation segments seem to bow out between obstacles to glide. At 700 °C, the obstacle distance l along the dislocations is about 100 nm. It decreases with decreasing temperature. In addition to these obstacles, the dislocations also contain jogs, labelled by J in Fig. 20a. Small dislocation dipoles, called "debris" and denoted by D, are created at these jogs. At decreasing temperature, slip also becomes increasingly inhomogeneous.

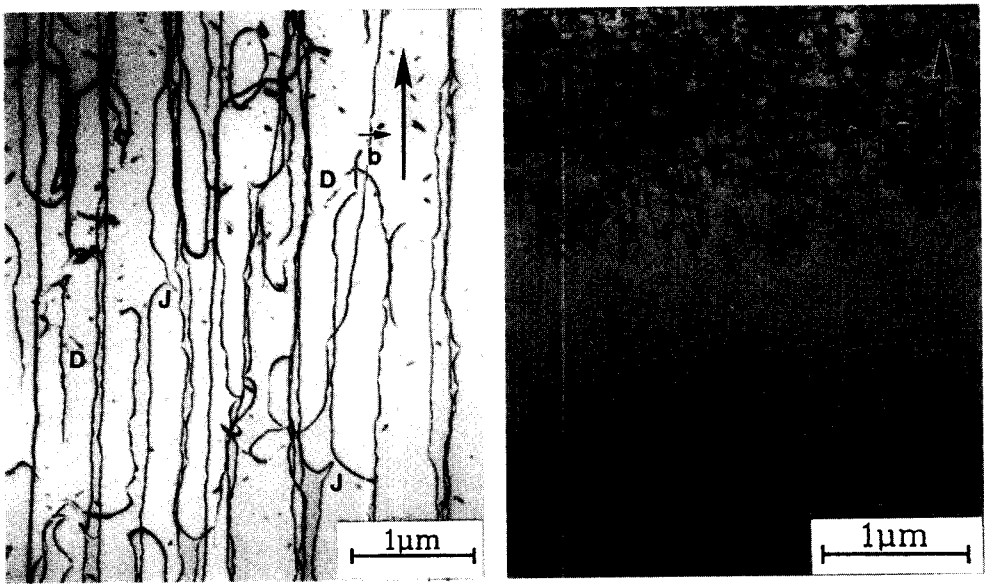

Fig. 20 Dislocation structure after deformation at low temperatures
a) 700 °C, (001) foil parallel to the primary slip plane. J jogs, D dipoles
b) 500 °C, cooled under load, ($\bar{1}$11) foil

Figure 20b shows that the dislocations are concentrated in relatively narrow slip bands. Similar features are observed at very low temperatures under confining pressure [18]. In contrast to high temperatures, the dislocation density drastically increases with temperatures decreasing below about 700 °C. Data taken from a few selected micrographs are plotted in Fig. 21. The values correspond to densities within the slip bands.

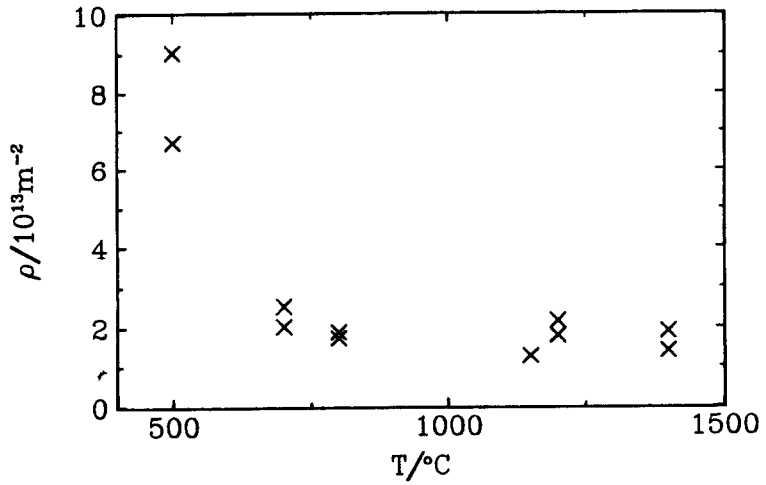

Fig. 21 Dependence of the dislocation density near the yield point on the deformation temperature (After [28])

4.4 Microstructure of Crystals Deformed in Orientations different from $[\bar{1}\,1\,\bar{2}]$

As described in Section 3.4, some experiments have been performed with compression axes different from $[\bar{1}\,1\,\bar{2}]$ to study the action of slip on planes other than {100}. After compression at 1400 °C along [001], the arrangement of edge pits on the {100} side faces in ⟨011⟩ directions can be explained by slip on either {110} or {111} planes [6]. The stereographic analysis of the slip steps at other directions of the compression axis seems to indicate that both systems have a similar resolved critical flow stress, which is about 20 % higher than that for slip on {100}. The orientation factor will then influence which of the systems will be activated. Only one TEM micrograph is published [13] of a specimen deformed along [001]. The dislocations are claimed to belong to {111} slip planes. X-ray topography of crystals deformed along [001] at 1400 °C points at the activation of slip on {110} planes [33]. Figure 22 shows a stereo pair of a respective specimen deformed also at 1400 °C. The careful evaluation of micrographs taken at different zone axes, as already described in Section 4.1, reveals that the dominating secondary planes are of {110} type.

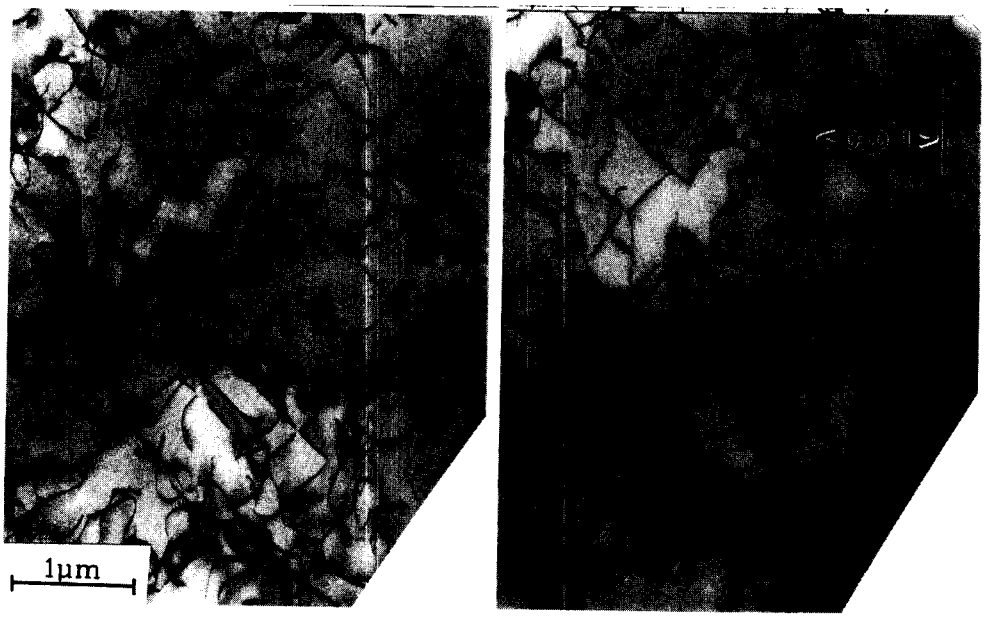

Fig. 22 Stereo pair of dislocation structure in ZrO_2-9.4mol%Y_2O_3 after deformation in ⟨001⟩ direction at 1400 °C, cooled under load. (010) plane

5. *In situ* Straining Experiments in the High-Voltage Electron Microscope

Recently, *in situ* straining experiments on zirconia single crystals were performed inside a HVEM, enabling the direct observation of the dislocation motion. A new high-temperature straining stage was used allowing temperatures above 1000 °C [34]. In addition to usual micrographs on photographic film, a video system can be used to record the dislocation motion. First results are described in [35 to 38]. These experiments may suffer from limitations owing to surface effects and to radiation damage. Surface effects prevent the formation of complex dislocation structures as in bulk specimens. Nevertheless, the kinematic behaviour of individual dislocations under load can well be observed. Visible radiation damage is rapidly produced at

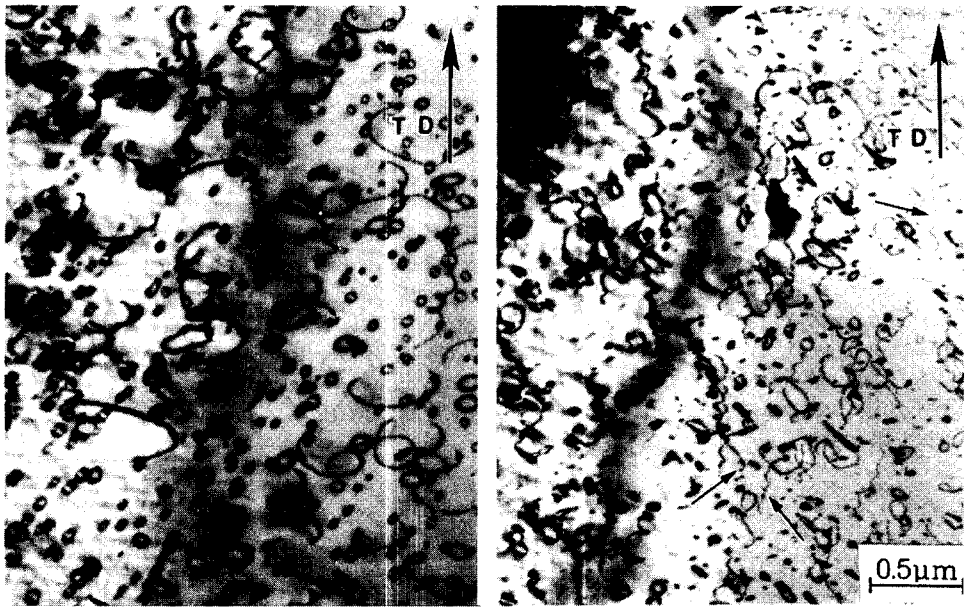

Fig. 23 Dislocation structures on the primary (001) plane in ZrO_2-9.4mol%Y_2O_3 during *in situ* deformation in the HVEM in $[\bar{1}1\bar{2}]$ direction. Foil plane $(\bar{1}11)$. a) Dislocations under load during deformation at about 1150 °C. b) During additional deformation at about 870 °C

temperatures slightly above room temperature [39] but disappears at higher temperatures. At about 750 °C a different type of very fine defects is generated, disappearing, however, above about 850 °C. Most experiments described below were carried out at about 1150 °C. There is no indication that these experiments are severely impaired by radiation damage.

Figure 23a shows the dislocation structure under load in a typical experiment at about 1150 °C and in $[\bar{1}1\bar{2}]$ tensile direction. These experiments correspond to conventional experiments in the intermediate temperature range described in Sections 3.2 and 4.2. At a $(\bar{1}11)$ foil normal dislocations are usually very instantaneously generated on the (001) primary slip plane. They are arranged either in bands of edge dislocations of a relatively high density of about $7.5 * 10^{13}$ m^{-2}, or as individual screw dislocations, as in Fig. 23a. The screw dislocations bow out between large jogs. As will be described in Section 7.2, the curvature of the bowed-out segments is a measure of the effective stress, which is a considerable part of the flow stress measured in the macroscopic experiments. Usually, the screw dislocations are not in a planar arrangement. In addition to the screw dislocations, many dislocation loops are formed, most probably by the double cross slip mechanism as indicated by the large number of jogs. These loops are slightly tilted out of the glide plane, i.e. they are glide loops with a small prismatic component. Their density is larger than that in the *post mortem* specimens (cf. Fig. 19). The stability of loops of a relatively wide range of sizes can only be explained by assuming some frictional force. During unloading they may collapse. The role of these loops for further deformation is not yet clear. At 1150 °C, the behaviour of dislocations on cube planes is mainly characterized by a very jerky motion over distances usually larger than those between dislocations, which corresponds to the athermal nature of the deformation revealed by macroscopic experiments in Section 3.2.

The specimen shown in Fig. 23a was cooled down to about 870 °C before it was further deformed at this temperature. Dislocations that move at the lower temperature like those marked by arrows in Fig. 23b are of curly shape which is typical of the action of localized obstacles, in accordance with the results of Section 4.3. The curvature is drastically larger than that at 1150 °C, corresponding to the increased stress.

In the HVEM, a single specimen with a (110) foil plane was deformed at 1150 °C along the $[\bar{1}1\bar{2}]$ tensile direction. In addition to edge dislocations on the primary (001) plane in almost perpendicular orientation to the foil plane, slip on a secondary non-cube plane, which has not been identified unequivocally, was activated as imaged in Fig. 24a. On this plane, the dislocations look similar to those on the cube plane but they move quite smoothly, indicating that a friction mechanism like the Peierls mechanisms is active on these planes, even at 1150 °C. Some samples were deformed in a ⟨100⟩ tensile direction, in which the resolved shear stress on the cube planes is zero. The dislocations, shown in Fig. 24b, move again smoothly, most probably on {110} planes.

Although until now the *in situ* experiments have been restricted to a small temperature range, they directly confirm the athermal nature of deformation on cube planes in the intermediate temperature range, the different dynamic behaviour of dislocations on cube and other slip planes, and the action of localized obstacles at lower temperatures.

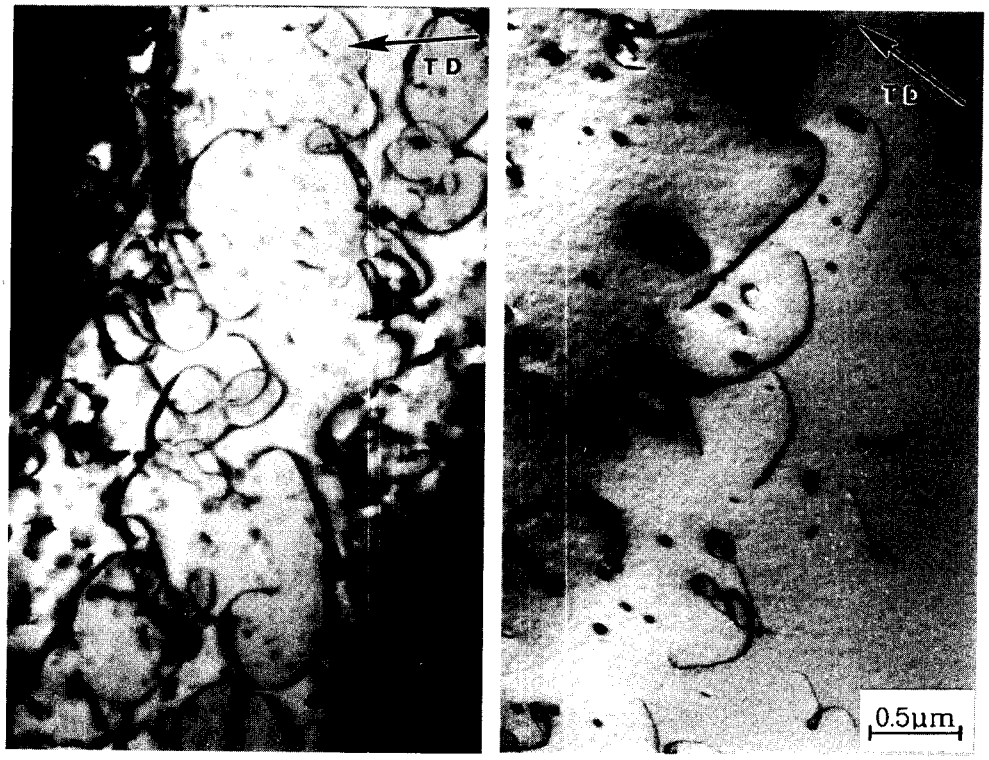

Fig. 24 Dislocations on non-cube planes in ZrO_2-9.4mol%Y_2O_3 during *in situ* deformation in the HVEM at about 1150 °C
a) Tensile axis $[\bar{1}1\bar{2}]$, foil plane (110). b) Tensile axis [100], foil plane (010)

6. Dislocation Velocity Measurements by the Stress Pulse Double-Etching Technique

The dependence of dislocation velocities on stress was measured between 1100 °C and 1450 °C by the stress pulse etching technique [40]. Fresh dislocations were introduced by Vickers hardness indentation at 800 °C. At the testing temperature, the indented specimens were loaded in four-point bending. The travelling distance of the dislocations was detected by selective etching. After the stress pulse, an asymmetry of the dislocation arrangement around the indentations on the tension and compression sides was explained by the internal stress field of the indentation. These internal stresses were not considered in the interpretation of the results. Different applied stresses were realized by evaluating indents in different positions between the inner and the outer supports, where the bending moment decreases linearly.

The velocities of edge and screw dislocations do not greatly differ within the investigated temperature range. Edge dislocations are slightly more mobile at lower temperatures while screw dislocations are faster at higher temperatures, in accordance with the fact that screw dislocations dominate in specimens deformed at low temperatures, and edge dislocations at high ones. The stress exponent m* can be obtained from double-logarithmic plots of the dislocation velocity versus stress, as shown in Fig. 25. At 1435 °C, m* is about 3 to 5, but at 1100 °C, m* = 1.4. The apparent activation energies calculated from Arrhenius plots of dislocation velocities against the reciprocal temperature amount to 5.0 ± 0.4 eV for edge dislocations and to 5.6 ± 0.6 eV for screws. The stress range of these measurements touches that of the macroscopic experiments only at the high-temperature end. A comparison with the macroscopic data reveals that at high temperatures both the stress exponent and the activation energies are of the same order of magnitude as the data for creep between 1400 °C and 1500 °C (see Table 2). As it will be described in Section 7.2, these data are interpreted by diffusion-controlled recovery and not by the dislocation mobility. The low-temperature end of the dislocation velocity data corresponds to the intermediate temperature range of Section 3.2. However, the stress range of the velocity measurements is far below the macroscopic flow stress. The strain rate sensitivity I can be calculated from the stress exponent m* by $I = \sigma / m^*$. The result for the highest stress σ = 185 MPa at 1100 °C and m* = 1.4 is I ≅ 130 MPa. This is clearly different from the very low values of I in the macroscopic deformation tests and the athermal nature of the dislocation motion in the *in situ* straining experiments in the intermediate temperature range. As stated in [40], the low

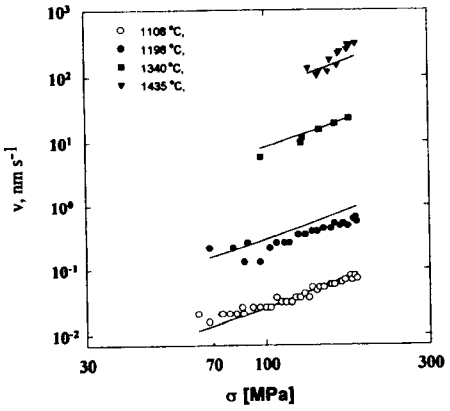

Fig. 25 Stress dependence of edge dislocation velocities at different temperatures in ZrO_2-9.4mol%Y_2O_3, measured by the stress pulse etching technique (After [40])

values of stress correspond to dislocation velocities which are more than 10 orders of magnitude smaller than those in other experiments. It may therefore be concluded that the dislocation velocity data do not describe the processes controlling the dislocation mobility in the macroscopic deformation experiments. Possibly, recovery of the internal stress field around the indentations has some influence on the dislocation motion. The different parameters can, however, also represent the intrinsic dislocation behaviour at low stresses, as it will be discussed below.

7. Interpretation and Discussion of the Experimental Results

In order to understand the mechanisms controlling the plastic deformation of cubic zirconia some properties of the defects in this material should be known.

7.1 Defect Structure in Cubic Zirconia

The properties of point defects influence the plastic deformation in many ways. At high temperature, dislocation climb is controlled by diffusion. Besides, the motion of dislocations may be impeded by point defect segregation or by the reorientation of defect clusters in the stress field of the dislocations. As all deformation data refer to yttria-stabilized zirconia, details of the following discussion are restricted to this material.

In order to conserve electrical neutrality, the incorporation of always two yttrium ions is accompanied with the formation of an anion vacancy. Thus, the high concentrations of stabilizing additives result in high concentrations of structural vacancies. Neutron scattering experiments have shown that these vacancies are not arranged randomly [10, 41]. The unit is a single vacancy with relaxed neighbours. These vacancies have a strong tendency to form vacancy pairs and a weak tendency to further aggregate to larger defects with $Zr_3Y_4O_{12}$ as the structural unit. The vacancy density seems to fluctuate after five {224} planes each with a correlation length of 0.4 nm for materials with 9.4 mol% Y_2O_3, and of 0.58 nm for such with 18 mol%. These correlated regions fill the space randomly. With respect to the time scale of the neutron scattering experiments, the aggregates are 'static' up to 1900 °C whereas single defects or small clusters may diffuse or reorient. With increasing yttria content, the lattice becomes gradually filled with the 'static' defects. This may explain why the ionic conductivity decreases at an yttria concentration above 8 mol% [42].

The stress-induced reorientation of defects of non-spherical symmetry can be studied by mechanical loss experiments. A composite internal friction peak was detected in ZrO_2-10mol%Y_2O_3 composed of two submaxima at 137 °C and 237 °C at 1 kHz [43]. The orientation dependence of the first maximum corresponds to a defect of trigonal ⟨111⟩ symmetry, which is supposed to be a dipole of a tetragonality between 0.12 and 0.14, consisting of an yttrium ion and an oxygen vacancy in nearest neighbour positions in ⟨111⟩ direction. This kind of association was also confirmed by extended x-ray absorption fine structure (EXAFS) measurements [44]. The maximum at a higher temperature may be due to aggregates of these dipoles. A knee in the Arrhenius plot of the ionic conductivity indicates that the dipoles should dissociate at higher temperatures, e.g. above about 520 °C in tetragonal zirconia polycrystals [45]. The transition temperature is higher in cubic zirconia having a higher yttria concentration. Recent mechanical loss measurements show that other relaxation peaks do not occur in ZrO_2-10mol%Y_2O_3 single crystals up to about 1200 °C [46]. The background damping increases above about 900 °C owing to diffusion-controlled viscoelastic deformation. The activation enthalpy of this high-temperature increase is 5.3 eV [46].

Dislocation climb processes at high temperatures require long-range diffusion in both sublattices. Zirconia exhibits very high diffusion coefficients for anion diffusion via oxygen vacancies. The activation energy of their motion is only of the order of magnitude of 1 eV (e.g. [47]). On the other hand, cation diffusion is quite slow. According to conventional diffusion studies, the activation energy of the self-diffusion of Zr^{4+} amounts to 4.05 eV, independent of the stabilizing additions [48]. The energies of the Y^{3+} self-diffusion and the Y - Zr interdiffusion are slightly higher [48, 49]. Nevertheless, the cation diffusion coefficient seems to depend on the yttria concentration. Dislocation loop shrinkage experiments between 1100 °C and 1300 °C (i.e. below the temperature range of conventional cation diffusion studies) proved cation diffusion in ZrO_2 with 18 mol% Y_2O_3 to be fifteen times slower than that in material with 9.4 mol% Y_2O_3 [50]. In both cases, the activation energy was equal to 5.3 eV, exactly the same value as that of the background damping in mechanical relaxation experiments. In the discussion based on the reaction rate model it is pointed out that a charged associate of a cation and an anion vacancy should be the mobile defect. The reduced diffusivity at a higher yttria content may be due to the increased trapping of mobile defects in accordance with the interpretation of the neutron scattering data above. As a consequence, climb processes of dislocations, which are controlled by the diffusion of the slower-moving species, will be determined by cation diffusion, which decreases with increasing yttria concentration.

In addition to intrinsic defects and those induced by the stabilizing additions, the zirconia crystals contain certain amounts of impurities. Usually, hafnium is present in the percent range. It is probably solved. Recently, it was detected that crystals of different yttria concentrations contain large amounts of nitrogen [51]. After deformation between 1600 °C and 1800 °C the latter appears in form of ZrN precipitates of up to more than 1 μm in size. These precipitates should influence the mechanical behaviour.

In summarizing the above it may be said that fully stabilized zirconia contains a large concentration of structural anion vacancies. Together with the stabilizer ions they may form some kind of short-range order, which may be stable within the range of the deformation experiments carried out up to now. Elastic dipoles cause mechanical loss at relatively tow temperatures. They should be dissolved at temperatures of most of the deformation studies. This is in contradiction to the postulated stability of defect aggregates up to high temperatures. Combined diffusion in both sublattices is governed by cation diffusion, depending on the concentration of the stabilizer. Very little is known about precipitates.

In order to calculate the elastic properties of dislocations, elastic constants are needed in the relevant temperature range. There are only two studies on cubic zirconia of different yttria contents, one up to 700 °C by an acoustic resonance technique [52], and the other up to about 1180 °C by Brillouin scattering combined with other methods [53]. The results for crystals of about 10 mol% Y_2O_3 are summarized in Fig. 26. Both measurements agree quite well at about 600 °C but show different temperature dependences. Extrapolation of the elastic constants to higher temperatures is difficult because of an anomaly at about 1000 °C posulated in [53]. Recent measurements, however, show a very weak decrease of the shear modulus between about 300 °C and 1200 °C [46].

Dislocation segments under load bow out in a characteristic way. The shape of these bowed-out segments can be described within the framework of the line tension approximation [54]. Line tension data were calculated after the procedure for anisotropic crystals in [55] using the elastic constants from [52] for 700 °C [56]. The resulting loop shapes are plotted in Fig. 27 for

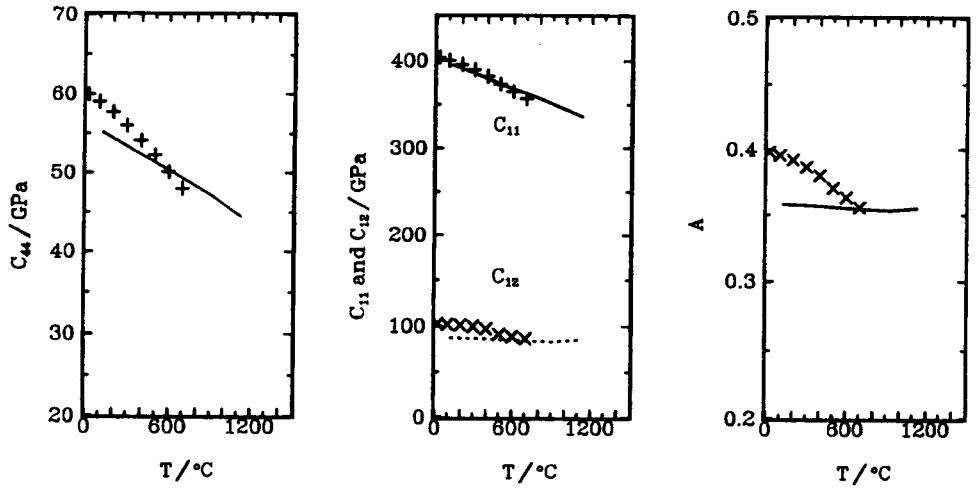

Fig. 26 Temperature dependence of elastic constants in ZrO_2-10mol%Y_2O_3. Data from [52], + and ×, and from [53], continuous line

dislocations on {001}, {110} and {111} planes. While the shape of the loops on the {111} plane is close to that expected for isotropic crystals, the loops on {110} planes show quite flat parts at the screw orientation. The dislocations on {001} planes are of angular shape with preferred orientations for mixed dislocations some degrees off the cube directions. Such preferred orientations have frequently been observed (cf. Fig. 19). The actual size of the loops depends on the local shear stress τ_b according to

$$y_o = K_s\, b / (4\,\pi\,\tau_b) \ln (l / \beta\, r_o) \qquad (6)$$

with y_o being the distance between the point where the screw dislocation cuts the y axis and the origin, i.e. the minor half axis of the loops, K_s, the so-called energy factor of a straight screw dislocation in anisotropic elasticity, b, the absolute value of the Burgers vector, l, the length of the bowing segment, r_o, an effective inner cut-off radius of the dislocations, and $\beta \cong 5$ a numerical constant relating the results of self-stress calculations of a dislocation bowing out between precipitates to a line tension analogon [57]. The numerical value of K_s for 700 °C is listed in Table 3, quoting also other parameters. Eq. 6 can be used to estimate the local stress from the curvature of bowed-out dislocation segments. These can be determined by fitting the

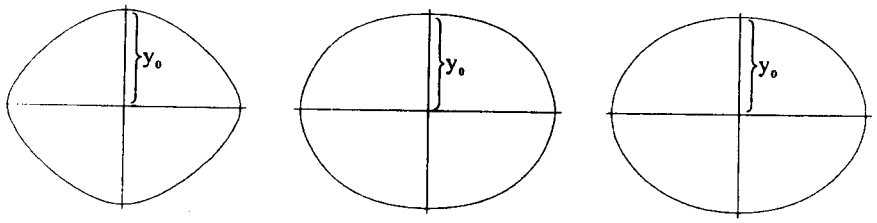

Fig. 27 Shape of dislocation loops under stress on the {001}, {110} and {111} planes. After [56]

calculated loop shapes of Fig. 27 in correct projection to the micrographs of the bowed-out segments to obtain individual values of y_o. Evaluating micrographs from *in situ* straining experiments yielded a back stress $\tau_b \cong 75 \pm 15$ MPa at 1150 °C and almost twice this value at 870 °C. The back stress values deduced from curved dislocation segments in macroscopic specimens cooled down under load are lower than those from *in situ* experiments. Hence, these micrographs represent a state already relaxed, in which the dislocation curvatures are different from those under deformation conditions.

7.2 Mechanisms Controlling the Flow Stress

In this section, a number of mechanisms will be discussed which may contribute to the flow stress of cubic zirconia. It will be tried to give, at least partly, a quantitative interpretation of the macroscopic data described in Section 3 for the different temperature ranges considering the microstructural observations outlined in Section 4. The discussion is based on the distinction between contributions to the flow stress τ by long-range (athermal) interactions between dislocations τ_i, and by short-range interactions τ^*, which result from thermally activated processes [58]

$$\tau = \tau_i + \tau^* \tag{7}$$

The contribution τ^* is also called the effective stress. If the thermally activated overcoming of obstacles contributes to the flow stress, τ^* is identical with the back stress τ_b mentioned above. It is not only τ^* that is responsible for the temperature dependence of the flow stress. Different dislocation structures generated during deformation at different temperatures may also result in a temperature dependence of τ_i, in addition to the influence of the temperature dependence of the elastic moduli.

Long-range interactions between parallel dislocations: An essential contribution to the athermal component τ_i of the flow stress results from long-range interactions of parallel dislocations, the so-called Taylor hardening [59]. It is based on the idea that dislocations on parallel slip planes have to pass dipole configurations in order to slip over longer distances. In isotropic elasticity, the shear stress one dislocation exerts on another one on a parallel slip plane of distance z_o may read

$$\tau = K\, b\, F(x/z_o) / (2\, \pi\, z_o) \tag{8}$$

with K being the shear modulus μ for screw dislocations and $\mu(1 - \nu)$ for edge dislocations, and $F(x/z_o)$, a dimensionless function of the position x of the second dislocation on its slip plane. The second dislocation can pass the stress field of the first one if the function F reaches its maximum value F_m. For screw dislocations there follows $F_{sm} = 0.5$ and for edge dislocations $F_{em} = 0.25$. Assuming that some average of the distance between the slip planes is related to the dislocation density ρ of the respective slip system by $1/z_o = \alpha\, \rho^{-1/2}$ yields an expression for the long-range contribution of parallel dislocations to the athermal component of the flow stress τ_i

$$\tau_p = \alpha\, K\, b\, F_m\, \rho^{1/2} / (2\, \pi) \tag{9}$$

α should amount to about 8. Though this formula does not very well represent the relation between the athermal flow stress component and the dislocation density over a wide range of parameters [60] it may be used to estimate τ_p in cubic zirconia.

As indicated in Table 3, zirconia shows a remarkable elastic anisotropy, entailing the problem of choosing suitable values of K and F_m in Eq. 8. In [28], it is shown by transforming the elastic constants to a coordinate system appropriate for the passing of dislocations with 1/2⟨110⟩ Burgers vectors on {001} and {111} slip planes (see, e.g., [61]) that the passing stress can still be described by Eq. (8) if K represents the energy factors of the respective dislocations and F_m numerical values characteristic of the anisotropic case. The data for screw and edge dislocations on {001} and {111} planes are listed in Table 3, demonstrating that screw dislocations generally interact somewhat more strongly than edge dislocations do, and that dislocations on the {111} slip system show a stronger hardening than those on {001}.

Table 3

Elastic constants c_{11}, c_{12}, and c_{44} of cubic zirconia at 700 °C from a regression analysis of data from [52], anisotropic energy factors of screw and edge dislocations K_s and K_e, and interaction constants for dislocation passing F_{sm} and F_{em} for slip on {001} and {111} planes for the same temperature from [28]

c_{11} [GPa]	c_{12} [GPa]	c_{44} [GPa]	A
356	85.7	47.9	0.355

plane	K_s [GPa]	K_e [GPa]	F_{sm} [GPa]	F_{em} [GPa]	K_sF_{sm} [GPa]	K_eF_{sm} [GPa]
{001}	80.4	97.8	0.30	0.20	24.0	19.3
{111}	80.4	112.3	0.66	0.31	53.0	34.6

Some values of dislocation densities in the intermediate and low-temperature ranges are displayed in Fig. 21. According to this, the dislocation density is almost constant at about $2*10^{13}$ m^{-2} above about 700 °C, rapidly increasing, however, below this temperature. Considering that glide of screw dislocations on {001} planes dominates the deformation at low temperatures, it may be estimated by Eq. 9 and the respective constants from Table 3 that the contribution τ_p of the interaction between parallel dislocations to τ_i is between 40 and 50 MPa above 700 °C and perhaps 100 MPa at 500 °C. This is about 40 % of the total critical (shear) stress in the intermediate temperature range, and about 30 % at 500 °C. For the high-temperature range (1400 °C), values of τ_p around 40 MPa should also follow from the dislocation densities in specimens cooled under load (also about $2*10^{13}$ m^{-2} as discussed in Section 4.1). As it will be discussed below, these densities are certainly reduced by recovery, thus not representing the situation during deformation.

Pinning of dislocations by large jogs: The *in situ* straining experiments at 1150 °C clearly show screw dislocations pinned by large jogs and bowing out between them (cf. Fig 23a). Dislocations with large jogs are also imaged in the *post mortem* specimen of Fig. 19, also taken in the intermediate temperature range. The large jogs result from cross slip, which is a prerequisite to dislocation multiplication. As obstacles to dislocation motion, they may only be overcome by bowing of the connecting dislocation segments through the critical (Frank-Read) configuration (in the model of isotropic line tension, it is the half-circle configuration) or by creating dislocation debris frequently observed if both arms adjoining the jog cannot pass each other. As these processes are of athermal nature, the back stress τ_b calculated from the curvature of the bowing segments in Section 7.1 causes a contribution to the athermal stress component τ_i. The stress relaxation experiments with very small values of the strain rate sensitivity I and very large values of m* as well as other results (cf. Section 3.2 and Fig. 11) suggest that the thermal component of the flow stress is very small in the intermediate temperature range. Thus, a theoretical prediction of the resolved flow stress may be

$$\tau = \tau_i = \tau_p + \tau_b = (45 + 75)\ \text{MPa}$$

With a flow stress in the intermediate temperature region of $\sigma_y \cong 250$ MPa (Figs. 7 and 10) and an orientation factor of 0.47 (Table 1), the observed microstructures allow a very good semiquantitative understanding of the deformation in this temperature range.

Jogs are created also at lower temperatures, as evidenced in Fig. 20a, in connection with cross slip and dislocation multiplication. Their concentration is, however, much lower than that of localized obstacles so that they do not significantly contribute to the flow stress. The latter is true for the high-temperature range, too. The distances between the jogs and the radius of curvature of the segments between them are so large that their contribution to the flow stress is very small.

Dislocation debris: As described above, large jogs produce dislocation debris if their height is smaller than a critical value for passing of the segments neighbouring the jogs (dipole opening criterion). This debris appears in the form of relatively short dislocation dipoles at low temperatures as in Fig. 20a. In the intermediate temperature range the dominating defects produced by the moving dislocations are the loops shown, e.g., in Fig. 23a. At high temperatures, long dislocation dipoles are pinched-off into dislocation loops by diffusion, particularly in the specimens cooled without load as in Fig. 15. The drag on the moving dislocations by the creation of these different kinds of debris is strong in the intermediate temperature range and was represented by the back stress τ_b. Most probably, it is small in the other temperature ranges. None of the micrographs proves that interactions between the moving dislocations and the debris play an important role in the deformation processes.

Dislocation Junctions: Dislocation junctions are created during multiple slip in the high-temperature range by interactions between dislocations of different Burgers vectors, according to the reaction in Eq. 5 of Section 4.1. This process leads to the formation of a three-dimensional dislocation network at high temperatures. In this network, macroscopic plastic flow may occur if the segments between the junctions bow out on a slip plane beyond the critical (Frank-Read) configuration, and afterwards slip over a distance approximately equal to the link length. In the respective creep model [62], the flow stress depends on the link length L via the Frank-Read criterion which, in the notation of the present paper, is represented by Eq. 6 with $y_0 = L/2$ and $l = L$. Using the experimental link length $L > 2.5\ \mu$m of Section 4.1, the contribution of the junctions to the flow stress is less than 14 MPa, i.e. dislocation reactions owing to multiple slip

do not contribute essentially to the flow stress in the high-temperature range. In all the other temperature ranges, single slip dominates in specimens deformed along $[\bar{1}\,1\,\bar{2}]$.

Elastic interaction between dislocations and point defects: As described in Section 7.1, cubic zirconia contains a very high concentration of the stabilizing aliovalent ions as well as of structural vacancies for charge compensation. Both may interact with the moving dislocations resulting in some kind of solution hardening depending on the concentration of the stabilizer. Such a dependence was proved in the high-temperature range as demonstrated in Fig. 3. Unfortunately, almost no data are available for the other temperature ranges. Neither are there any theoretical estimations of the interaction energies between dislocations and individual point defects. In most other materials these energies are smaller than 1 eV, which restricts the interaction to temperatures below about 300 °C, i.e. these interactions do certainly not contribute to the flow stress in the high-temperature range.

As already pointed out in Section 7.1, cubic zirconia exhibits mechanical loss peaks at 137 °C and 237 °C due to stress-induced reorientation of yttria ion-vacancy dipoles and aggregates of them. These phenomena may give rise to contributions to the flow stress by reorientation in the stress field of moving dislocations, the so-called induced Snoek effect. According to the temperatures of the loss maxima, the induced Snoek effect might be of importance at the lowest temperatures discussed in this paper. It usually causes transient effects after changes of the deformation rate. These effects do not occur at the low temperatures, but between about 600 °C and 1000 °C. They are documented in Figs. 12 and 13. This is a temperature range in which, according to measurements of the ionic conductivity, the dipoles should already be dissociated. However, there is a discrepancy between these conductivity data and the neutron scattering experiments which suggest short-range ordered structures to be stable up to high temperatures. Thus, the transient effects might be due to a stress-induced reorientation of larger complexes. Respective maxima were, however, not observed in mechanical relaxation studies at higher temperatures [46].

The transient effects can alternatively be interpreted by changes in the mobile dislocation density after changes of the deformation conditions. As the dislocation density certainly reacts more slowly on changes of the deformation conditions than the dislocation velocity, the instantaneous response differs from the steady state one yielding the transient effects. The enhanced glide after a small load increment out of a very low strain rate as demonstrated in Fig. 13 seems to be an expression of the athermal nature of the deformation in this temperature range. A small load increase activates a number of existing dislocation sources, however, glide is quickly stopped by work hardening or exhaustion of the sources.

Anyway, the stress increments owing to the transient effects, e.g. after stress relaxation, are always small compared with the flow stress. They are therefore not very important. Thus, it may be concluded that elastic interactions between dislocations and isolated point defects as well as small clusters never play an important role in the deformation of cubic zirconia.

Interaction between dislocations and localized obstacles (precipitates): The zig-zag shape of dislocations after deformation at low temperatures as in Fig. 20 and the curly shape of dislocations under load during *in situ* straining at 870 °C of Fig. 23b point at the action of strong localized pinning as the main origin of the low-temperature increase of the flow stress of Figs. 7 and 10. A few of these pinning points are clearly identified as jogs by their trailing of dipoles like those labelled J in Fig. 20a. The majority, however, seem to be so-called localized obstacles. As

discussed above, isolated point defects or small aggregates do not seem to essentially contribute to the flow stress. Therefore, the localized obstacles most certainly consist of small precipitates. The nature of these precipitates is not clear, yet. Perhaps, nitrogen is involved. The thermally activated overcoming of the localized obstacles may also give rise to the strong increase of the strain rate sensitivity of the flow stress below 1000 °C, demonstrated in Fig. 8.

A semiquantitative interpretation of the deformation data between 700 °C and 1150 °C was given in [7] in terms of the model of thermally activated overcoming of small precipitates. In this model, the plastic strain rate $\dot{\varepsilon}$ is given by an Arrhenius equation of the dislocation velocity v

$$\dot{\varepsilon} = \rho_m \, b \, v = \rho_m \, b \, v_0 \exp(-\Delta G(\tau^*) / kT) = \dot{\varepsilon}_0 \exp(-\Delta G(\tau^*) / kT) \tag{10}$$

$$\text{with} \quad \Delta G = \int_{x_1}^{x_2} (f(x) - l \, b \, \tau^*) \, dx = \Delta F(\tau^*) - l \, b \, d \, \tau^* \tag{11}$$

Here, $\dot{\varepsilon}_0 = \rho_m \, b \, v_0$ is the pre-exponential factor containing a constant v_0 and the mobile dislocation density ρ_m, ΔG, the Gibbs free energy of activation, k, the Boltzmann constant, and T, the absolute temperature. f(x) is the force the obstacle exerts on the dislocation depending on the position of the dislocation with respect to the obstacle, the so-called force-distance profile of the obstacle. x_1 and x_2 are the equilibrium positions of the dislocations on the entrance and exit sides of the obstacle. l is the obstacle distance along the dislocation, and b, the absolute value of the Burgers vector. The result of the integration is the right part of Eq. 11, where ΔF is the Helmholtz free energy of activation, and $d = x_2 - x_1$, the activation distance. It is an effective "thickness" of the obstacle depending on τ^*. The product l b d is related to the experimental activation volume by

$$V = kT / (\Phi I) = (2/3) \, l \, b \, d \tag{12}$$

where Φ is the orientation factor after Table 1 ($\Phi = 0.47$ for the $(001)[1\bar{1}0]$ slip system under consideration). The factor 2/3 originates from the Friedel statistics of randomly arranged strong obstacles. The activation parameters V and ΔG can be determined from the strain rate and temperature sensitivities of the flow stress I and $-\Delta\sigma/\Delta T$ described in Sections 3.1 and 3.3. The use of the left side of Eq. 12 is based on the assumption that changes of the mobile dislocation density do not affect the determination of the strain rate sensitivity I. Therefore, in the range of transient effects appearing (600 °C to 1000 °C) the instantaneous stress increment after a strain rate change was used in Eq. 2, but not the steady state one. As an example, values characteristic of 700 °C were discussed in [7]. With I = 7.8 MPa the activation volume amounts to about 80 b^3. Using $l \cong 100$ nm $\cong 300$ b from Section 4.3, the activation distance d becomes about 0.4 b. This is a value quite compatible with obstacles surmountable by thermal activation.

The experimental activation energy Q_e can be obtained from the temperature sensitivity $-\Delta\sigma/\Delta T$ and the strain rate sensitivity I of the flow stress by using Eq. 4. Respective data are contained in Figs. 8 and 9. At 700 °C, $Q_e \cong 7.2$ eV. According to [63], Q_e represents the activation enthalpy ΔH, but neither ΔG nor ΔF. ΔG can be calculated from ΔH by considering the activation entropy. In [63], a formula is derived on the assumption that the entropy originates solely from the temperature dependence of the shear modulus. For the $(001)[1\bar{1}0]$ slip system the proper modulus is c_{44}. Using a regression analysis of c_{44} versus temperature of the data from [52] (cf. Fig. 26)

yields a Gibbs free energy of activation $\Delta G \cong 3.3$ eV at 700 °C and a strain rate of 10^{-6} s^{-1}. This value is again consistent with the model.

The temperature dependence of the flow stress and of the strain rate sensitivity is discussed in [7] on the basis of a model potential for localized obstacles proposed in [64]

$$\Delta G(\tau^*) = (\mu/\mu_0)\, \Delta F_0\, [1 - (\mu_0\, \tau^*/\mu\, \tau_0)^{1/2}]^{3/2} \qquad (13)$$

μ (= c_{44}) is the shear modulus depending on temperature, μ_0, its value at a reference temperature, ΔF_0, the total activation free energy at zero stress, and τ_0, the flow stress contribution of the localized obstacles at zero temperature. Eq. 13 can be inserted into Eq. 10 yielding expressions for the temperature dependence of I and τ^*. An appropriate regression of I versus T and the value of $\Delta G = 3.3$ eV quoted above lead to $\tau_0 = 760$ MPa, whereas a regression of τ versus T yields $\tau_0 = 990$ MPa. Although these values do not entirely coincide, the agreement seems to be satisfactory. The total activation energy should be $\Delta F_0 \cong 4.3$ eV. The model suggests that the interaction between dislocations and precipitates becomes unimportant above 1000 °C to 1270 °C, in agreement with all observations. The evaluation was limited to the temperature range between 700 °C and 1150 °C. Besides, the athermal part of the flow stress τ_i was considered to depend on the temperature only through the shear modulus, i.e. disregarding the increase of the dislocation density with decreasing temperature (cf. Fig. 21). A more sophisticated evaluation of the data available at present requires a potential which is more narrow than that of Eq. 13 at high stresses, but this does not alter the general conclusions. It is therefore argued that the interaction between dislocations and localized obstacles is the main contribution to the thermal part τ^* of the flow stress in the temperature range between about 600 °C and 1000 °C although the respective precipitates are not yet identified. The back stress τ_b of curved dislocations is identical to the (thermally activated) effective stress τ^*, while the long-range part of the flow stress τ_i is given by the interaction between parallel dislocations τ_p. Accordingly,

$$\tau = \tau_i + \tau^* = \tau_p + \tau_b$$

At the lower end of this temperature range, τ^* should amount to about 70 % of the whole flow stress.

Peierls mechanism: Usually, the lattice friction, which is also called the Peierls mechanism, controls the dislocation mobility at low temperatures. In the present case of ZrO_2-9.4mol%Y_2O_3, between 600 °C and 400 °C the strain rate sensitivity I of Fig. 8 increases by about one order of magnitude. Below 400 °C it is perhaps constant at about 200 MPa. This value corresponds to an experimental activation volume of only 2 b^3. These features are well consistent with the action of the Peierls mechanism for glide on {001} planes at the lowest end of the investigated temperature range.

In [65] it is tried to give a quantitative analysis of the low-temperature deformation data by superposing the action of localized obstacles and the Peierls mechanism. The Gibbs free energy of activation of Eq. 11 is then replaced by

$$\Delta G = \int_{x_1}^{x_2} (f(x) - \{8\, \Gamma\, [U_p(x) + \tau^*\, b\, h]\}^{1/2})\, dx \qquad (14)$$

with Γ being the line tension, $U_p(x)$, the Peierls potential, and h, a measure of the bowing of the segment between two localized obstacles. If the Peierls mechanism is active h takes some dynamical value, which is smaller than the equilibrium value determined by the line tension for the case only localized obstacles are active. The quantitative conclusions of the model in [65] are not discussed here because, among other things, the dependence of the athermal component τ_i of the flow stress on the temperature has not been considered, which is due to the strong increase of the dislocation density with decreasing temperature. Nevertheless, the qualitative predictions of the model suggest that the Peierls stress is a remarkable contribution to the flow stress at very low temperatures. This is also evident from the weak dependence of the strain rate sensitivity on the stress, expressed in the shape of the stress relaxation curve at 400 °C in Fig. 11. It is still open whether the importance of the Peierls stress for glide on {001} planes is restricted to low temperatures, or not. The dislocation velocity data determined in [40] between 1200 °C and 1435 °C at very low stresses, outlined in Section 6, can easily be interpreted in terms of the Peierls model. This may neither contradict the very jerky character of the dislocation motion in the intermediate temperature range, as evidenced by the *in situ* experiments of Section 5, nor the parameters of deformation on {001} planes in the respective temperature range. For the very low dislocation velocities, the limiting temperature for the Peierls mechanism will be shifted to higher temperatures. Some kind of lattice friction can also explain that dislocation loops of round shape are stable although they are smaller than a critical size depending on the actual stress. These loops have particularly been observed in the *in situ* experiments.

At intermediate temperatures the critical flow stress on non-cube planes is about twice as high as that on the cube plane, as described in Section 3.4. This difference is certainly due to differences in the lattice resistance. This is consistent with a relatively smooth dislocation motion observed on non-cube planes during *in situ* straining in the HVEM at 1150 °C (cf. Section 5). It may therefore be concluded that a remarkable Peierls stress suppresses the activation of glide on non-cube planes at low temperatures in most orientations of the compression axis. At temperatures between 1200 °C and 1400 °C the Peierls stress on non-cube planes should become insignificant.

Recovery-controlled creep: This subsection aims at interpreting the plastic properties of c-ZrO_2 in the high-temperature range. In this range, the work-hardening rate is generally very small after the initial rise of the stress before the macroscopic yield point. Thus, a steady state is almost reached in the constant strain rate experiments, with the deformation behaviour very similar to that under creep conditions at the same strain rate.

The discussion above allows one to conclude that the dislocations are very mobile on the cube planes at temperatures above about 1100 °C. They are less mobile on other planes, but the difference is already small at 1400 °C (cf. Sections 4.4 and 5). The microstructures observed by TEM at room temperature do not clearly evidence the mechanisms controlling the flow stress. The densities of large jogs and of dislocation junctions are too low to remarkably influence the flow stress. Similarly, the total dislocation density in specimens cooled under load describes a contribution of about 40 MPa to the flow stress by Taylor hardening. This low value of the dislocation density for explaining the flow stress by mutual dislocation interactions is consistent, however, with results on many other materials under creep conditions. As discussed in [66], the flow stress in creep experiments is related to the dislocation density by an equation like Eq. 9 but with a numerical constant α F_m / (2 π) twice the value used above for work-hardening conditions.

The difference between dislocation structures in specimens cooled under load and such cooled without load as, e.g., the different dislocation densities, the relaxation of large parts of the load in relatively short times as well as the pinching-off of dislocation dipoles hint at recovery processes taking place at high temperatures. Other authors (e.g. [27]) explain the high-temperature plastic properties by dislocation network models including recovery. The particular theory [67], however, is based on viscous dislocation motion, which strongly contradicts the stress relaxation behaviour discussed below.

The high-temperature plasticity of ZrO_2 can be interpreted on the basis of the phenomenological model described in [68, 69], as already pointed out in [23]. The kinetic law, i.e. the dependence of the strain rate $\dot{\varepsilon}$ on the effective stress τ^*, which is represented by the Arrhenius relationship of Eq. 10, may be approximated by the power law

$$\dot{\varepsilon} = \dot{\varepsilon}_0 (\tau / \tau_0)^m \tag{15}$$

τ_0 is a threshold stress related to the long-range stress component τ_i, $\dot{\varepsilon}_0$, a constant, and m, the kinetic stress exponent, not identical with the experimental stress exponent m* defined in Eq. 3. The change of the microstructure during straining is described by an evolution law

$$d\tau_0/d\varepsilon = \Theta_0 \{1 - C \tau_0 \dot{\varepsilon}^{-1/n}\} \tag{16}$$

where Θ_0 is the initial work-hardening coefficient, C, a constant, and n, the strain-softening exponent. This evolution law considers dynamic recovery. Under steady state conditions as in creep, τ_0 is constant so that

$$\dot{\varepsilon}_{SS} = C \tau_0^n = C' \tau^{n'} \tag{17}$$

with $1/n' = 1/n + 1/m$. This is the well known steady state creep law. Eqs. 15 and 16 describe also transient phenomena like stress relaxation. At the beginning of relaxation, the relaxation behaviour is dominated by the kinetic law with the slope of the relaxation curve in a double-logarithmic plot being equal to the kinetic exponent m. A respective plot of the data of the first relaxation curves of Fig. 6, showing "inverse" curvature, yields very high values of m (up to 100) like the m* values in the intermediate temperature range. This again points at the athermal nature of the dislocation motion. The tail of the relaxation curves at low strain rates, however, is dominated by the strain-softening exponent n, which turns out to be close to 4 or somewhat larger. It is of the same order of magnitude as the experimental stress exponents m* measured in creep and listed in Table 2.

In conclusion, the thermally activated character of the deformation processes at high temperatures results from thermally activated recovery processes rather than from processes controlling the dislocation mobility. The recovery processes effectively reducing the dislocation density require dislocation climb and, consequently, diffusion in both sublattices. The activation energy of deformation should therefore be equal to that of the slower cation diffusion. Respective values are discussed in Section 7.1. While this energy from conventional diffusion studies is only somewhat larger than 4 eV, loop shrinkage experiments yield 5.3 eV in accordance with mechanical loss measurements. These values have to be compared with the creep energies of Table 2, which are all remarkably higher. Note that the creep energies are apparent energies in that sense that a 1/T term usually appearing in creep equations has not been considered so that the true activation

energies of creep will be somewhat lower. It has still to be checked whether this will dissolve the discrepancy, or not. An important feature of high-temperature deformation is the dependence of the flow stress on the yttria content. This can be explained by the strong decrease of the diffusion coefficient with increasing yttria concentration, observed in the loop shrinkage experiments, and should therefore not be caused by solution or precipitation hardening.

7.3 Open Problems

The following problems are worth further investigating:

The effects on the deformation behaviour of the possible change from the fluorite crystal structure to the primitive cubic one below 800 °C are not yet clear. The absolute value of the Burgers vectors has to be determined for specimens deformed at a sufficiently low temperature.

The information on the slip planes active in addition to cube planes is contradictory. At low temperatures, the planes operative during deformation along ⟨001⟩ have not yet been determined unambiguously. At high temperatures, {100}, {110} and {111} planes may probably occur as secondary planes. It is still controversial whether mainly {100} planes, or the other ones, are activated as secondary planes during deformation in ⟨112⟩ direction.

Almost no data are available on the mechanical properties of cubic zirconia with other stabilizers than yttria. Up to now, the influence of the yttria concentration on the deformation behaviour has been investigated solely in the high-temperature range. Measurements at lower temperatures are highly desirable. They may help decide whether the explanation of the concentration dependence of the flow stress at high temperatures via an influence on the cation diffusion coefficient is correct, or not. The only data available contained in Figs. 8 and 10 suggest that the low-temperature plasticity is relatively insensitive to the content and type of the stabilizer.

The nature of the localized obstacles acting below about 900 °C has not yet been analyzed. The respective precipitates are most probably small and of low density. They are therefore difficult to trace by electron microscopy methods.

The activation energy of high temperature deformation seems to be higher than that of cation diffusion. A more careful analysis is necessary to find out whether this discrepancy can be explained on the basis of the existing models.

8. Conclusions

Plastic deformation in yttria stabilized cubic zirconia occurs by the motion of dislocations of 1/2 ⟨110⟩ Burgers vectors. It is controlled by different processes in different temperature ranges.

At intermediate temperatures around 1100 °C, single slip on a cube plane dominates the deformation along ⟨112⟩ and is of athermal nature. The magnitude of the flow stress can semiquantitatively be explained by the long-range interaction between parallel dislocations and by the back stress of dislocations bowing out between large jogs.

At decreasing temperatures, the flow stress and the strain rate sensitivity strongly increase. The respective thermally activated part of the flow stress is due to localized obstacles, most probably small precipitates. In addition, the increase of the dislocation density with decreasing temperature

causes the athermal contribution owing to long-range interactions between parallel dislocations to rise, too.

Below about 500 °C the activation volume becomes only a few b^3 indicating the action of the Peierls mechanism on cube planes in conjuction with precipitation hardening and long-range interactions.

On non-cube planes, however, the higher resolved flow stress and the viscous dislocation motion at 1150 °C suggest that the Peierls stress is active up to about 1400 °C.

Above about 1200 °C, the cube plane of largest orientation factor acts as the primary slip plane. Secondary slip is activated in the course of deformation. After some strain, all 1/2 ⟨110⟩ Burgers vectors possible are observed. Recovery processes taking place during deformation cause the flow stress to become strain rate sensitive again. The deformation behaviour can be described by usual creep equations. However, the activation energy is most probably greater than the energy of cation diffusion. A definite creep model cannot be proposed, yet. The link length between dislocation junctions does not seem to control the flow stress.

Acknowlegdements

The authors are grateful to Professors A.H. Heuer and M. Rühle as well as to Doctor M. Bartsch for stimulating discussions. The work done on zirconia at the MPI in Halle was supported by the Deutsche Forschungsgemeinschaft.

References

[1] Th. Profen, R.B. Neder, F.Frey, and W. Assmus, Acta Cryst. B **49**, 599 (1993).
[2] Th. Profen, R.B. Neder, F.Frey, D.A. Keen and C.M.E. Zeyen, Acta Cryst. B **49**, 605 (1993).
[3] E. Fries, F. Guiberteau, A. Dominguez-Rodriguez, D.S. Cheong, and A.H. Heuer, Philos. Mag. A **60**, 107 (1989).
[4] D.S. Cheong, A. Dominguez-Rodriguez and A.H. Heuer, Philos. Mag. A **60**, 123 (1989).
[5] D.S. Cheong, A. Dominguez-Rodriguez and A.H. Heuer, Philos. Mag. A **63**, 377 (1991).
[6] A. Dominguez-Rodriguez, D.S. Cheong and A.H. Heuer, Philos. Mag. A **64**, 923 (1991).
[7] B. Baufeld, M. Bartsch, U. Messerschmidt, and D. Baither, Acta metall. mater. **43**, 1925 (1995).
[8] B. Baufeld, M. Bartsch, D. Baither, and U. Messerschmidt, to be published
[9] M. Morinaga, H. Adachi and M. Tsukada, J. Phys. Chem. Solids **44**, 301 (1983).
[10] R. Osborn, N.H. Anderson, K. Clausen, M.A. Hackett, W. Hayes, M.T. Hutchings, and J.E. MacDonald, Mater. Sci. Forum **7**, 55 (1986).
[11] A.G. Evans and P.L. Pratt, Philos. Mag. **31**, 1213 (1969).
[12] R.J. Keller, T.E. Mitchell and A.H. Heuer, Acta metall. **36**, 1061 (1988).
[13] A. Dominguez-Rodriguez and A.H. Heuer, Cryst. Lattice Defects and Amorph. Mater. **16**, 117 (1987).
[14] A. Dominguez-Rodrigues and A.H. Heuer, Rad. Eff. and Def. in Solids **119-121**, 759 (1991).
[15] R.E. Carter and W.L. Roth, in: Electromotive Force Measurements in High-Temperature Systems, ed. by C.B. Alcock, Inst. of Mining & Metall., London 1968, pp. 125-144

[16] K.J. McClellan, S.-Q. Xiao, K.P.D. Lagerlöf, and A.H. Heuer, Philos. Mag. A **70**, 185 (1994).
[17] P. Teracher, H. Garem and J. Rabier, Euroceramics **3**, Engineering Ceramics, ed. by R.A. Terpstra and R. Meetselaar, Elsevier, London and New York 1989, p. 3.334
[18] P. Teracher, H. Garem and J. Rabier, in: Strengh of Metals and Alloys, ed. by D.G. Brandon, R. Chaim and A. Rosen, Freund Publs. London 1991, p. 217
[19] B. Baufeld, M. Feuerbacher and D. Baither, unpublished results
[20] B. Baufeld, D. Baither, M. Bartsch, and U. Messerschmidt, to be published
[21] K.J. McClellan, A.H. Heuer and L.P. Kubin, to be published in Acta metall. mater. (1996).
[22] A. Dominguez-Rodriguez, K.P.D. Lagerlöf and A.H. Heuer, J. Amer. Ceram. Soc. **69**, 281 (1986).
[23] U. Messerschmidt, B. Baufeld, K.J. McClellan, and A.H. Heuer, Acta metall. mater. **43**, 1917 (1995).
[24] M. Jiménez-Melando, J. Martinez-Fernández, A. Dominguez-Rodriguez, and J. Castaing, J. Europ. Ceram. Soc. **12**, 97 (1993).
[25] J. Martinez-Fernández, M. Jiménez-Melando, A. Dominguez-Rodriguez, and A.H. Heuer, Euroceramics Vol. 3, ed. by G. deWith, R.A. Terpstra and R. Metsellar, Elsevier Appl. Sci., London and New York 1989, p. 3.318
[26] J. Martinez-Fernández, M. Jiménez-Melando, A. Dominguez-Rodriguez, and A.H. Heuer, J. Amer. Ceram. Soc. **73**, 2452 (1990).
[27] D. Goméz-Garcia, J. Martinez-Fernández, A. Dominguez-Rodriguez, P. Eveno, and J. Castaing, Acta mater. **44**, 991 (1996).
[28] B. Baufeld, Doctoral Thesis, Halle (Saale) 1996
[29] J. Lankford, J. Mater. Sci. **21**, 1981 (1986).
[30] U. Messerschmidt, B. Baufeld, D. Baither, and M. Bartsch, 4th Eurocermaics, Vol. 3, ed. by S. Meriano and V. Sergo, Gruppo Editoriale Faenza Editrice, 1995, p. 479.
[31] P. Teracher, Ph.D. Thesis, Poitiers 1990
[32] G. Morscher, P. Pirouz and A.H. Heuer, J. Amer. Ceram. Soc. **74**, 491 (1991).
[33] F. Guiberteau, F.L. Cumbrera, A. Dominguez-Rodriguez, E. Fries, and J. Castaing, J. Appl. Cryst. **27**, 406 (1994).
[34] U. Messerschmidt and M. Bartsch, Ultramicroscopy **56**, 163 (1994).
[35] U. Messerschmidt, B. Baufeld, D. Baither, M. Bartsch, K.J. McClellan, and A.H. Heuer, in: Strength of Materials, ed. by H. Oikawa, K. Maruyama, S. Takeuchi, and M. Yamaguchi, The Japan Institute of Metals 1994, p. 741.
[36] B. Baufeld, U. Messerschmidt, M. Bartsch, and D. Baither, Key Eng. Mater. **97/98**, 431 (1994).
[37] B. Baufeld, U. Messerschmidt, D. Baither, M. Bartsch, A. Foitzik, and M. Rühle, in: Plastic Deformation of Ceramics, ed. by R.C. Bradt, C.A. Brooks, and J. Routbort, Plenum Press, New York and London 1995, p. 43.
[38] U. Messerschmidt, B. Baufeld, D. Baither, and M. Bartsch, in preparation for Mater. Sci. Eng.
[39] B. Baufeld, D. Baither, U. Messerschmidt, M. Bartsch, and I. Merkel, J. Amer. Ceram. Soc. **76**, 3163 (1993).
[40] B. Ya. Farber, A.S. Chiarelli, and A.H. Heuer, Philos. Mag. A **72**, 59 (1995).
[41] N.H. Andersen, K. Clausen, M.A. Hackett, W. Hayes, M.T. Hutchings, J.E. MacDonald, and R. Osborn, Physica **136B**, 315 (1986).

[42] O.T. Sorensen, ∅. Johannesen and K. Clausen, in: Transport-Structure Relations in Fast Ion and Mixed Conductors, ed. by F.W. Poulson, N.H. Andersen, K. Clausen, S. Skaarup, and O.T. Sorensen, Riso 1985, p. 93.
[43] M. Weller, Z. Metallkunde **84**, 6 (1993).
[44] C.R.A. Catlow, A.V. Chadwick, G.N. Greaves, and L.M. Moroney, J. Am. Ceram. Soc. **69**, 272 (1986).
[45] M. Weller and H. Schubert, J. Am. Ceram. Soc. **69**, 573 (1986).
[46] M.Weller, Stuttgart, private comminication (1996).
[47] Y. Oishi and K. Ando, in: Transport in Nonstoichiometric Compounds, ed. by G. Simkovic and V.S. Stubican, Plenum Publ., 1985, p. 189.
[48] Y. Oishi, K. Ando, and Y. Sakka, in: Advances in Ceramics, ed. by M.F. Yang and A.H. Heuer, Vol. 7, Am. Ceram. Soc., Westerville OH 1989, p. 208.
[49] H. Solman, J. Chaumont, C. Dolin, and C. Monty, Ceram. Trans. **24**, Am. Ceram. Soc., Westerville OH 1991, p. 175.
[50] F.R. Chien and A.H. Heuer, Philos. Mag. A **73**, 681 (1996).
[51] D. Gomez-Garcia, J. Martinez-Fernandez, A. Dominguez-Rodriguez, and K.H. Westmacott, submitted to Phil. Mag. Letters (1996)
[52] H.M. Kandil, J.D. Greiner and J.F. Smith, J. Am. Ceram. Soc. **67**, 342 (1984).
[53] P.J. Botha, J.C.H. Chiang, J.D. Comins, P.M. Mjwara, and P.E. Ngoepe, J. Appl. Phys. **73**, 7268 (1993).
[54] G. DeWitt and J.S. Koehler, Phys. Rev. **116**, 1113 (1959).
[55] D.M. Barnett, R.J. Asaro, S.D. Gavazzi, D.J. Baconm and R.O, Scattergood, J. Phys. F: Metal Phys. **2**, 854 (1972).
[56] D. Baither, unpublished work
[57] R.O. Scattergood and D.J. Bacon, Philos. Mag. **31**, 179 (1975).
[58] A. Seeger, in: Handbuch der Physik, ed. by S. Flügge, Vol. VII, 1, Springer-Verlag, Berlin, Göttingen, Heidelberg 1955.
[59] G.J. Taylor, Proc. Roy. Soc. **A145**, 362 (1934).
[60] S.J. Basinski and Z.S. Basinski, in: Dislocations in Solids, Vol. 4, ed. by F.R.N. Nabarro, North-Holland Publ., Amsterdam 1979, p. 261.
[61] J.P. Hirth and J. Lothe, Theory of Dislocations, John Whiley and Sons, New York 1982
[62] H.E. Evans and G. Knowles, Acta Metall. **25**, 963 (1977).
[63] G. Schoeck, Phys. Status Solidi **8**, 499 (1965).
[64] U.F. Kocks, A.S. Argon and M.F. Ashby, in: Thermodynamics and Kinetics of Slip, Progress in Mater. Sci. Vol. 19, Pergamon Press, Oxford 1975.
[65] B. Petukhov, M. Bartsch, B. Baufeld, D. Baither, and U. Messerschmidt, to be published
[66] S. Takeuchi and A.S. Argon, J. Mater. Sci. **11**, 1542 (1976).
[67] B. Burton, Philos. Mag. A **45**, 657 (1982).
[68] U.F. Kocks, J. Eng. Mater. Technol. **98**, 76 (1976).
[69] U.F. Kocks, Physical Basis for Non-Elastic Constitutive Relations, Discussion paper at Symp. Adv. in Metal Deformation, Cornell Univ., Ithaca NY 1976